

Identifying Chemical Aerosol Signatures using Optical Suborbital Observations: How much can optical properties tell us about aerosol composition?

5 Meloë S. F. Kacenelenbogen¹, Qian Tan^{1,2}, Sharon P. Burton³, Otto P. Hasekamp⁴, Karl D. Froyd⁵,
Yohei Shinozuka^{1,2}, Andreas J. Beyersdorf⁶, Luke Ziemba³, Kenneth L. Thornhill³, Jack E. Dibb⁷,
Taylor Shingler⁸, Armin Sorooshian⁸, Reed W. Espinosa^{9,10}, Vanderlei Martins¹⁰, Jose L. Jimenez⁵,
Pedro Campuzano-Jost⁵, Joshua P. Schwarz¹¹, Matthew S. Johnson¹, Jens Redemann¹², Gregory L.
Schuster³

10 ¹NASA Ames Research Center, Moffett Field, CA, 94035, USA

²Bay Area Environmental Research Institute (BAERI), Moffett Field, CA, 94035, USA

³NASA Langley Research Center, Hampton, VA, 23666, USA

⁴SRON, Netherlands Institute for Space Research, Utrecht, 3584, Netherlands

⁵Cooperative Institute for Research in Environmental Sciences (CIRES), University of Colorado, Boulder, CO, 80309, USA

15 ⁶California State University, San Bernardino (CSUSB), San Bernardino, CA, 92407, USA

⁷University of New Hampshire, Durham, NH, 03824, USA

⁸University of Arizona, Tucson, AZ, 85721, USA

⁹NASA Goddard Space Flight Center, Greenbelt, MD, 20771, USA

¹⁰University of Maryland Baltimore County (UMBC), Baltimore, MD 21250, USA

20 ¹¹Chemical Sciences Division, NOAA Earth System Research Laboratory, Boulder, CO, USA

¹²University of Oklahoma, Norman, OK 73019, USA

Correspondence to: Meloë S.F. Kacenelenbogen (meloe.s.kacenelenbogen@nasa.gov)

Abstract. Improvements in air quality and Earth's climate predictions require improvements of the
25 aerosol speciation in chemical transport models, using observational constraints. Aerosol speciation (e.g.,
organic aerosols, black carbon, sulfate, nitrate, ammonium, dust, or sea salt) is typically determined using
in situ instrumentation. Continuous, routine aerosol composition measurements from ground-based
networks are not uniformly widespread over the globe. Satellites, on the other hand, can provide a
maximum coverage of the horizontal and vertical atmosphere but observe aerosol optical properties (and
30 not aerosol speciation) based on remote sensing instrumentation. Combinations of satellite-derived
aerosol optical properties can inform on Air Mass aerosol Types (AMTs). However, these AMTs are
subjectively defined, might often be misclassified and are hard to relate to the critical parameters that
need to be refined in models.

In this paper, we derive AMTs that are more directly related to sources and hence to speciation. They are
35 defined, characterized, and derived using simultaneous *in situ* gas-phase, chemical and optical
instruments on the same aircraft during the Study of Emissions and Atmospheric Composition, Clouds,
and Climate Coupling by Regional Surveys (SEAC⁴RS, an airborne field campaign carried out over the
US during the summer of 2013). We find distinct optical signatures for AMTs such as biomass burning

(from agricultural or wildfires), biogenic and polluted dust. We find that all four AMTs, studied when prescribed using mostly airborne *in situ* gas measurements, can be successfully extracted from a few combinations of airborne *in situ* aerosol optical properties (e.g., extinction angstrom exponent, absorption angstrom exponent and real refractive index). However, we find that the optically based classifications for biomass burning from agricultural fires and polluted dust include a large percentage of misclassifications that limit the usefulness of results related to those classes.

The technique and results presented in this study are suitable to develop a representative, robust and diverse source-based AMT database. This database could then be used for widespread retrievals of AMTs using existing and future remote sensing suborbital instruments/networks. Ultimately, it has the potential to provide a much broader observational aerosol data set to evaluate chemical transport and air quality models than is currently available by direct *in situ* measurements. This study illustrates how essential it is to explore existing airborne datasets to bridge chemical and optical signatures of different AMTs, before the implementation of future spaceborne missions (e.g., the next generation of Earth Observing System (EOS) satellites addressing Aerosol, Cloud, Convection and Precipitation (ACCP) designated observables).

1 Introduction

Aerosols have an important yet uncertain impact on the Earth's radiation budget (e.g., Boucher et al., 2013) and human health (e.g., US EPA, 2011, 2016; Lim et al., 2012; Lanzi, 2016; Landrigan et al., 2018; Wu et al., 2020). In particular, aerosols impact human health by increasing the number of cases of emphysemas, lung cancers, diabetes, hypertension and premature deaths (e.g., Wichmann et al., 2000; Pope et al., 2002; Lim et al., 2012; Lelieveld et al., 2019, 2015; Stirnberg et al., 2020; Nault et al., 2021); this particularly holds true for specific species of aerosols with high oxidative potential (e.g., Daellenbach et al. 2020).

We define aerosol speciation as the inherent chemical composition of the aerosol, the chemical species that are represented in Chemical Transport Models (CTMs) (e.g., black carbon (BC), organic aerosol (OA, typically classified into primary, and secondary organic aerosol, SOA), brown carbon, sulfate, nitrate, ammonium, dust, sea salt). These are typically defined to match the operational quantities reported by *in situ* instruments.

CTMs derive aerosol optical properties and estimate the Radiative Forcing due to aerosol-radiation interactions (RFari), based on simulated water uptake, simulated aerosol mass concentrations, simplified aerosol size distributions and assumed aerosol refractive indices per species (Chin et al., 2002). RFari for individual aerosol species are less certain than the total RFari (Boucher et al., 2013; Myhre et al., 2013). Myhre et al. (2013) present a large AeroCom Phase II inter-model spread in the RFari of several aerosol species. BC, for example, had a 40% relative standard deviation in RFari. Inter-model diversity in estimates of RFari is caused in part by different methods for estimating aerosol properties (e.g., emissions, transport, chemistry, deposition, optical properties (Loeb and Su, 2010)), and to a lesser extent by surface and cloud albedos, water vapor absorption, and radiative transfer schemes (e.g., Randles et al., 2013; Myhre et al., 2013; Stier et al., 2013; Thorsen et al., 2021).

In order to constrain model simulations, and in particular to reduce the uncertainties associated to RFari per species, data assimilation techniques have been adopted using optimal estimation methods and observational constraints that we separate in four main groups. The first group of constraints consists in column-integrated aerosol optical properties from passive orbital and/or suborbital instruments (e.g., Collins et al., 2001; Yu et al., 2003; Generoso et al., 2007; Adhikary et al., 2008; Niu et al., 2008; Zhang et al., 2008; Benedetti et al., 2009; Schutgens et al., 2010; Kumar et al., 2019; Tsikerdekis et al., 2021). The second group consists in fine aerosol mass concentrations from airborne and/or ground-based instruments (e.g., Lin et al., 2008; Pagowski and Grell, 2012). The third group consists in a combination of *in situ* gas-phase measurements (e.g., sulfur dioxide, nitrogen dioxide (NO₂), ozone and carbon monoxide (CO)), fine aerosol mass concentrations from ground-based instruments and column-integrated aerosol optical properties from passive orbital instruments (e.g., Ma et al., 2019). The fourth group consists in surface (e.g., Kahnert, 2008, Yumimoto et al., 2008; Uno et al., 2008) and space-based aerosol lidar profiles (e.g., Sekiyama et al., 2010; Zhang et al., 2011), which are used to constrain aerosol mass and extinction. Constraining model-predicted aerosol mass concentrations with passive satellite total column-integrated aerosol properties has been shown to be useful to constrain model-predicted Aerosol Optical Depth (AOD). This is the case for the single-channel visible AOD retrievals from the Moderate Resolution Imaging Spectroradiometer (MODIS) sensor (e.g., Yu et al., 2003; Zhang et al., 2008; Benedetti et al., 2009; Sessions et al., 2015; Buchard et al., 2017; Kumar et al., 2019; Ma et al., 2019). However, this process does not correct the uncertainty associated with the simulated vertical distribution of aerosols, nor can it derive aerosol chemical speciation. On the other hand, assimilation of satellite-derived optical properties related to particle size (e.g., Extinction Angstrom Exponent, EAE) and light absorption (e.g., Single Scattering Albedo, SSA) represents a step forward (e.g., Tsikerdekis et al., 2021). Another way to improve estimates of speciated RFari would be to use satellite-derived total column speciated aerosol mass concentration to adjust the mass concentration of individual aerosol masses when applying data assimilation techniques in the model (and potentially the emission/chemistry/transport processes driving them). However, currently no satellite-derived retrievals of aerosol chemical speciation exist.

Let us note an important distinction between what is called aerosol speciation and Air Mass Aerosol Type (AMT). The AMT is representative of typical aerosol mixes associated with certain seasons and geographical locations. It is a coarse definition (qualitative) of the aerosol size, shape and color that dominates an air mass (e.g., clean marine, dust, polluted continental, clean continental, polluted dust, smoke, and stratospheric in the case of the active spaceborne Cloud-Aerosol Lidar with Orthogonal Polarization (CALIOP) on board the Cloud-Aerosol Lidar and Infrared Pathfinder Satellite Observation (CALIPSO) (Omar et al., 2009)).

In the next paragraphs, we concentrate on A-Train's POLDER (Polarization and Directionality of Earth's Reflectances) passive satellite observations on board the PARASOL platform. POLDER measures polarized radiances in 14-16 viewing directions at 443, 670 and 865 nm and retrieves aerosol optical properties over land (Deuzé et al., 2001) and over ocean (Herman et al., 2005) using its standard retrieval algorithm. In addition, two alternate POLDER retrieval algorithms from the SRON-Netherlands Institute for Space Research algorithm (Hasekamp et al., 2011, Fu et al., 2020) and generated by the GRASP (Generalized Retrieval of Atmosphere and Surface Properties) algorithm (Dubovik, 2014) make full use of multi-angle, multi-spectral polarimetric data.

120 On the one hand, recent techniques infer aerosol speciation from POLDER using an inverse modeling
framework, which consists in fitting satellite observations to model estimates by adjusting aerosol
emissions. For example, Chen et al. (2018, 2019) use POLDER/GRASP spectral AOD and Aerosol
Absorption Optical Depth (AAOD) to estimate e.g., emissions of desert dust, or BC. Similarly,
125 Tsikerdekis et al., (2021) use POLDER/SRON AOD, AAOD, EAE and SSA, but with a different model
and assimilation technique, and to estimate the aerosol mass and number mixing ratio of specific aerosol
species.

On the other hand, AMTs inferred by various techniques and using satellite remote sensing observations
are useful to provide spatial context (e.g., regional, seasonal, annual trends) to support other observations
of aerosols and clouds or evaluate other aerosol type classifications. These AMTs are also useful in
130 evaluating models in simple cases where a single aerosol species is present (e.g., “pure dust”). For
example, Johnson et al. (2012) demonstrated how CALIOP mineral dust aerosol extinction retrievals were
applied to improve dust emission and size distribution parameterizations in the global GEOS-Chem
model, a global 3-D model of atmospheric chemistry driven by meteorological input from the Goddard
Earth Observing System (GEOS).

135 We have inferred qualitative AMTs from passive POLDER/SRON remote-sensing retrievals of EAE
between 491 and 863 nm, SSA at 491 nm, a difference in Single Scattering Albedo, dSSA between 863nm
and 491 nm, a Real Refractive Index, RRI at 670 nm and a pre-Specified Clustering and Mahalanobis
Classification method (SCMC) (Russell et al., 2014).

The SCMC method, based on the methodology developed by Burton et al. (2012), uses the Mahalanobis
140 distance (Mahalanobis, 1936) analysis in multidimensional space to assign AMTs based on a suite of
observed parameters. The number of parameters is adjustable, as are the nature of the parameters
themselves. Similarly, the AMT definitions are flexible. However, a key requirement for the SCMC
method is that reference values for each AMT must be defined (i.e., the mean, variances and covariances
of the aerosol variables), typically using prescribed AMTs for a subset of observations. In practice, when
145 applying SCMC to a new environment, a training data set is created by prescribing a set of air masses
based on independent observations. Those pre-specified AMTs from Russell et al. (2014) are based on
dominant aerosol types from AEROSOL ROBOTIC NETWORK (AERONET) stations at specific locations and
times (Holben et al., 1998). In Russell et al. (2014), qualitative AMTs were derived over the island of
Crete, Greece, during a 5-year period using the SCMC method and pre-specified AMTs from global
150 AERONET observations. We refer the reader to section 2 of Russell et al. (2014) or Burton et al. (2012)
for a thorough description of the SCMC method.

We have extended the methods of Russell et al. (2014) (i.e., over Greece) to the entire globe for the year
2006. On the one hand, the POLDER-derived AMTs presented reassuring features such as (i) dust over
155 the Atlantic between the Saharan coast and Central to South America, predominant from March to August,
(ii) urban industrial aerosols found near industrialized cities such as the East Coast of North America and
over South East Asia, and (iii) two different types of Biomass Burning (BB) over the South East Atlantic
(i.e., one illustrating more smoldering combustion and pre-specified using AERONET stations located in
South America and the other one illustrating more flaming combustion and using AERONET stations in
160 Africa). We found darker BB (i.e., lower SSA) in August compared to September, due to an increase of

POLDER-retrieved SSA during the season, reflecting either a change in BB aerosol composition (Eck et al., 2013) or a mix of AMTs (Bond et al., 2013).

On the other hand, many features such as marine aerosols over the Saharan Desert or urban industrial aerosol type in South America, were most likely misclassified. Ambiguities in POLDER-derived AMTs could result from a combination of four factors:

- (i) Errors in POLDER reflectance/polarization measurements and aerosol retrievals (e.g., errors in POLDER retrievals get larger for smaller AODs and/ or a smaller range of scattering angles),
- (ii) A coarse spatial resolution of the gridded POLDER product (e.g., $2^\circ \times 2^\circ$),
- (iii) Non-optimal AERONET-based pre-specified AMTs used as a training dataset (e.g., the AMT illustrating more flaming combustion is defined in locations, such as Mongu in Africa, where smoldering and flaming combustion might be occurring at the same time, together with other AMTs present in the atmospheric column) and/or
- (iv) A restricted number of POLDER-derived aerosol optical parameters. That is, the relative AMT discriminatory power increases with the number and diversity of observed parameters.

Unlike in Russell et al. (2014), where we used total column remote sensing-inferred optical properties which are often representative of a mix of different AMTs, the AMTs in this study are defined, characterized, and derived using simultaneous gas-phase, chemical and optical instruments on the same aircraft. This reduces errors in measurements/retrievals and errors due to spatio-temporal colocation (see i-ii above). It also reduces ambiguities in the selection of the AMT training dataset (see iii), and we specifically investigate the strengths and weaknesses of optical properties used as tools to define AMTs and how much these optical properties can capture dominant aerosol speciation (see iv).

The objectives of this study are to:

- Prescribe well-informed AMTs that display distinct aerosol chemical and optical signatures to act as a training AMT dataset, and
- Evaluate the ability of airborne *in situ* measured aerosol optical properties that are suitable to be retrieved from space to successfully extract these AMTs.

We first describe the instruments, observations and methods used in this study (section 2). We provide additional information on the methods in Appendix A.1. We then present (section 3), conclude (section 4) and discuss (section 5) our results. We provide additional results in Appendix A.2. We refer the reader to Appendix B for the abbreviations and acronyms used in this paper.

2. Data and Method

2.1. Instruments and Observations

We select NASA DC-8 airborne *in situ* data collected during the Study of Emissions and Atmospheric Composition, Clouds, and Climate Coupling by Regional Surveys (SEAC⁴RS) project (Toon et al., 2016), which was carried out in August–September 2013 over North America with a strong focus on the

200 Southeastern US (SEUS). Measurements are collected at the altitude of the aircraft and are not
representative of the full column satellite retrieval. Although these airborne *in situ* observations lack the
widespread coverage of surface networks or satellite retrievals, their benefits include measuring a wide
variety of gas-phase species, aerosol types and aerosol optical properties (Toon et al., 2016). A major
strength of our study is the use of *in situ* gas-phase, chemical and optical instruments on the same NASA
205 DC-8 research aircraft during the SEAC⁴RS campaign. Table 1 lists the various airborne *in situ*
instruments, products used in this study and important references for each instrument. It also shows that
the instruments in Table 1 sample different aerosol sizes. This is especially true for the DASH-SP
instrument, which sampled particles with dry diameters between 180 and 400 nm during SEAC⁴RS
(Shingler et al., 2016). In contrast, the sampled air was provided to the PI-Neph instrument through the
NASA LARGE shrouded diffuser inlet, which sampled isokinetically and is known to have a 50% passing
210 efficiency at an aerodynamic diameter of at least 5 μm at low altitude (McNaughton et al., 2007; Espinosa
et al., 2017).

Instruments		Products	Sampled Aerosol Size	References
1	PTR-MS, DACOM, TD-LIF, NO _y O ₃	Acetonitrile, isoprene, monoterpene, Carbon Monoxide (CO), Nitrogen dioxide (NO ₂)	-	PTR-MS (Mikoviny et al., 2010); DACOM (Fried et al., 2008); TD-LIF (Cleary et al., 2002); NO _y O ₃ (Ryerson et al., 2012)
2	PALMS	Internally mixed Sulfate/Organic/ Nitrate (SON), Biomass Burning (BB), Sea salt, and Dust particle types	<5µm dry diameter	Murphy et al., 2006 Froyd et al., 2019
3	SAGA	Chloride (Cl), Bromide (Br), Nitrate (Nit.), Sulfate (Sul.), Oxalate(C ₂ O ₄), Sodium (Na), Ammonium (Amm.), Potassium (K), Magnesium (Mg), Calcium (Ca.)	<4µm dry diameter	Dibb et al., 2003
4	AMS	Organic Aerosol (OA), Sulfate, Ammonium, Nitrate	0.02 - 0.8 µm (trapezoidal transmission efficiency, D50 at 0.035 and 0.35 µm)	DeCarlo et al., 2006; Canagaratna et al., 2007; Hu et al., 2015; Guo et al., 2021
5	SP2	Black Carbon (BC)	0.1-0.5µm (BC component, only)	Perring et al., 2017
6	LARGE TSI and PSAP	Absorption, Scattering and Extinction Coefficient (AC, SC and EC) at 450, 550 and 700 nm	<5µm dry diameter for Dry Total Scattering Coefficients at 450, 550, and 700 nm (TSI Neph) and Total Absorption Coefficients at 467, 530 and 660 nm (PSAP)	Ziemba et al., 2013; McNaughton et al., 2007
7	DASH-SP	Real Refractive Index (RRI) at 532nm	0.18-0.40µm dry diameter	Sorooshian et al., 2008; Shingler et al., 2016
8	PI-Neph	RRI at 532 nm	<5 µm dry diameter	Dolgos and Martins, 2014; Espinosa, 2017, 2018

215 **Table 1: Instruments, products, sampled aerosol size, and references relevant to this study. More**
information on the instruments during SEAC⁴RS can be found here:
<https://espo.nasa.gov/home/seac4rs/content/Instruments>.

220 In this study, we use the sixteen aerosol optical parameters listed in Table 2 (i.e., five first parameters at
three wavelengths or three combinations of wavelengths and last parameter at 532nm) and derived from
the optical instruments in line 6-8 of Table 1.

	Initial Names	What We Call Them in This Study	Calculation
1	AC	AC	$AC_{\lambda 1} = EC_{\lambda 1} - SC_{\lambda 1}$
2	EAC	Extinction Angstrom Exponent (EAE)	$EAC_{\lambda 1, \lambda 2} = -\ln(EC_{\lambda 1} / EC_{\lambda 2}) / \ln(\lambda 1 / \lambda 2)$
3	AAC	Absorption Angstrom Exponent (AAE)	$AAC_{\lambda 1, \lambda 2} = -\ln(AC_{\lambda 1} / AC_{\lambda 2}) / \ln(\lambda 1 / \lambda 2)$
4	SSAC	Single Scattering Albedo (SSA)	$SSAC_{\lambda 1} = SC_{\lambda 1} / EC_{\lambda 1}$
5	dSSAC	Difference in SSA at $\lambda 1$ and $\lambda 2$ (dSSA)	$SSAC_{\lambda 1, \lambda 2} = SSAC_{\lambda 1} - SSAC_{\lambda 2}$
6	RRI	Real Refractive Index (RRI)	-

Table 2: *In situ* optical parameters used in this study (provided at a given aircraft altitude by the instruments in line 6-8 of Table 1), the way we call them in this paper, and how they are computed. The way we call these parameters is closer to what would be observed from remote sensing instruments. In the calculations, $\lambda 1$ and $\lambda 2$ are two given wavelengths. In this paper, we compute (i) SSA and AC at 450, 550 and 700 nm, (ii) EAE, AAE and dSSA between 450-550, 550-700 and 450-700 nm and (iii) RRI at 532 nm.

Instead of simply using the standardized SEAC⁴RS merged dataset, a lot of effort was dedicated to carefully collocate, combine, cloud-screen, filter, humidify datasets (i.e., convert from dry to ambient conditions), as well as compute and interpolate/extrapolate optical parameters to specific wavelengths (see section A.1.1 and A.1.2 in the appendix).

2.2. Method

Figure 1 illustrates the overall method in this study, which involves following the five steps described below.

(1) Prescribe Source-based Aerosol air Mass Types (called PS-AMT)

The PS-AMTs are defined using the gas-phase and aerosol instruments in line 1-2 of Table 1 and a method based on Espinosa et al. (2018) and Shingler et al. (2016) illustrated in Fig. 2. These aerosol and gas measurements better characterize the aerosol properties in these AMTs compared to observations of aerosol optical properties. First, we define Polluted Dust PS-AMT (called “**PollDust**”) using PALMS dust number fraction (i.e., PALMS 'MineralFrac_PALMS') above 0.15 and the integrated dry aerosol volume concentration by the TSI Aerodynamic Particle Sizer (APS) above $2 \mu\text{m}^3 \text{cm}^{-3}$ (i.e., 'IntegV_Daero-PSL_APS_LARGE'; note that APS measurements sampled dry aerodynamic diameters ranging from 0.56 to $6.31 \mu\text{m}$ (Espinosa et al., 2018)). Similarly, we define **Marine** PS-AMTs when PALMS sea-salt number fraction > 0.15 and total volume $> 2 \mu\text{m}^3 \text{cm}^{-3}$. The remaining observations may then be evaluated for **BB** PS-AMTs using PTRMS “Acetonitrile”, WAS “Isoprene_WAS”, PTRMS “Isoprene-Furan”, PTRMS “Monoterpenes”, WAS “CO_WAS” and DACOM “CO_DACOM” if (i) acetonitrile $> 250 \times 10^{-3}$ ppbv, or (ii) (acetonitrile $> 190 \times 10^{-3}$ ppbv) & (acetonitrile/(isoprene + monoterpene) > 2.5) or (iii) CO > 250 ppbv. BB PS-AMTs are further differentiated as coming from

255 agricultural fires (called “**BBAg.**”) if the longitude is east of -95° or from wildfires (called “**BBWild.**”) if
the longitude is west of -95° . The -95° longitude threshold was selected according to the location of
agricultural fires in Liu et al. (2016). If observations are not classified as PollDust or BB, we classify
them as biogenic (called “**Bio.**”) if isoprene + monoterpene > 2 ppbv. Finally, remaining observations are
classified as **Urban** if the altitude is below 3km and $\text{NO}_2 > 1$ ppbv (i.e., using the NOAA Nitrogen Oxides
260 and Ozone (NO_yO_3), NO_2 _ESRL or TDLIF “ NO_2 _TDLIF”). Section 3.1 describes these PS-AMTs, their
location and composition during SEAC⁴RS.

(2) Determine most useful and well separated aerosol optical properties

Once the PS-AMTs are defined, we test whether these PS-AMTs exhibit distinct aerosol optical properties
265 and then, select the most useful and well separated aerosol optical properties. This step, as well as the
following steps, use the optical parameters listed in Table 2 and provided by the instruments listed in lines
6-8 of Table 1. To select the most useful and well separated aerosol optical properties for each PS-AMT,
we define a cluster in multi-dimensional parameter space, which is composed of all the data points (values
of optical properties) in that PS-AMT category. Then, for each point in the data set, we calculate the
270 nearest cluster using the Mahalanobis distance (Mahalanobis, 1936). If the nearest cluster to a point
corresponds to the PS-AMT, then that point is “steady”. This method was used in previous studies (e.g.,
Espinosa et al. (2018)) and is described in further detail in section A.1.3 in the appendix. Section 3.2
describes the results from this step i.e., the most useful and well separated aerosol optical properties in
our study.

275

(3) Define optical-based training classes (called DO-Class)

We use the set of aerosol optical parameters defined in the second step above to define optical-based class
definitions (called DO-Class), including means, variances and covariances. In other terms, in this step,
we form the mathematical definitions of the classes. The DO-Class use the “steady” (i.e., well separated)
280 points from the first half of all valid aerosol optical observations. Once the training clusters DO-Class are
defined, we use the Mahalanobis distance to filter outliers from our training dataset and further “purify”
them. Similar to Russell et al. (2014), we delete points that have less than 1% probability of belonging to
each pre-specified DO-Class. We also delete from a specified cluster any points that are closer (in terms
of Mahalanobis distance) to a different cluster. Note that unlike in Russel et al. (2014), this additional
285 filtering step has a minimal impact on the training dataset in our study.

(4) Derive Optical-based Aerosol air Mass Types (called DO-AMT)

The DO-AMTs are analyzed and classified using the set of aerosol optical properties defined in the second
step above, the DO-Class defined in the third step and the SCMC method for a set of observations that
290 was not included in the training data sets. This test data set is based on independent observations and must
be of the same nature than the training dataset. In this study, our test dataset is composed of independent
airborne *in situ* optical properties. It is the other half of all valid aerosol optical observations (DO-Class
are defined using the “steady” portion of the first half). We derive DO-AMT to each test data point using
the SCMC method and the DO-Class. This is achieved by assigning the test datapoint to the DO-Class
295 that shows minimum Mahalanobis distance in a multi-dimensional space made of the best suited and most
separable optical properties. Section 3.3 describes the results from this step.

(5) Compare Derive Optical-based (DO-AMT) and Prescribe source-based AMTs (PS-AMT)

We evaluate the ability of airborne aerosol optical properties to successfully extract PS-AMTs by comparing PS-AMTs and DO-AMTs. Section 3.4. describes the results of this final step in our study.

In Fig. 1, we illustrate AMTs as wolves, and their optical properties as their tracks. The second and third step consist in describing the optical properties (or tracks) of each AMT (or wolf). The fourth step consists in inferring an AMT (or wolf) from its optical properties (or tracks). The fifth and last step consists in comparing the inferred to the initial AMT (or wolf).

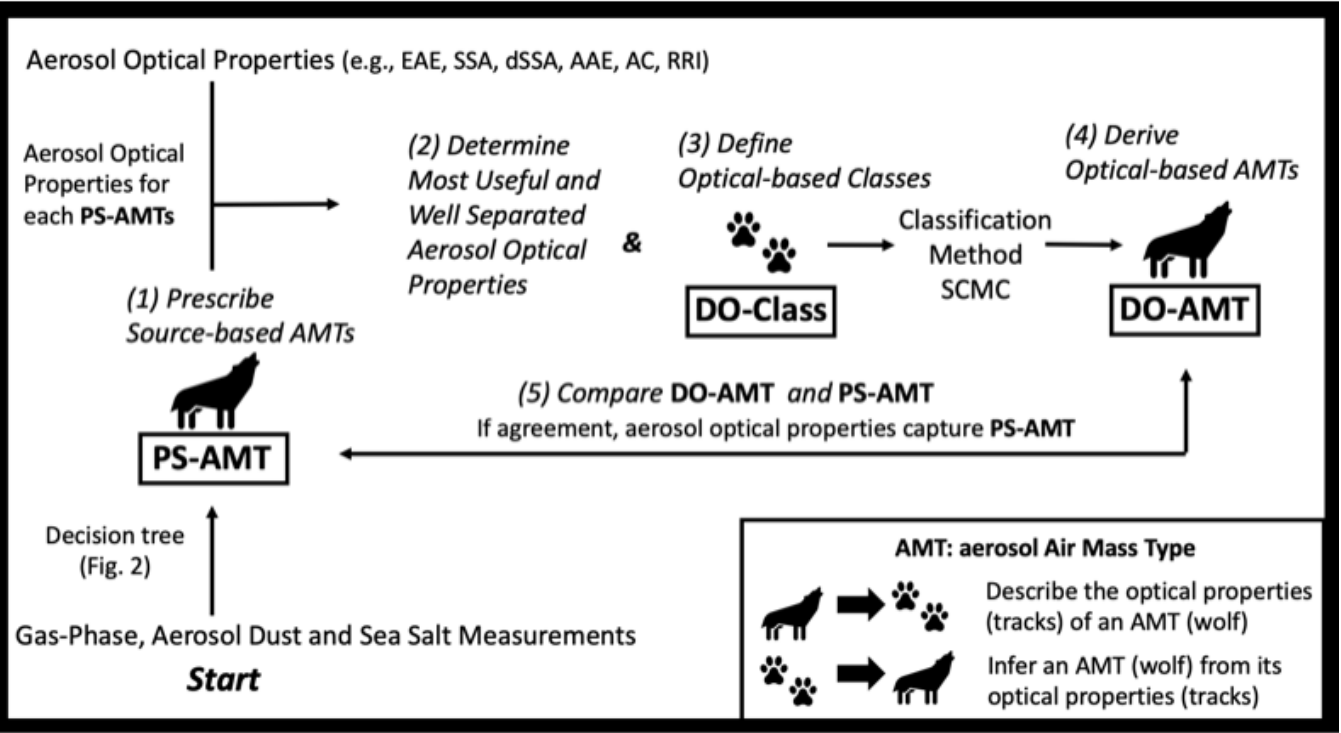


Figure 1: Overall method in this study; PS-AMTs: Prescribed Source-based Air Mass Types (AMTs); DO-Class: Defined Optical-based Class definitions and DO-AMTs: Derived Optical-based AMTs; EAE: Extinction Angstrom Exponent; SSA: Single Scattering Albedo; dSSA: difference in SSA; AAE: Absorption Angstrom Exponent; AC: absorption coefficient; RRI: real Refractive Index; SCMC: pre-Specified Clustering and Mahalanobis Classification. The concept of the wolf and its tracks is based on the dragon and its tracks in Bohren and Huffman (1983).

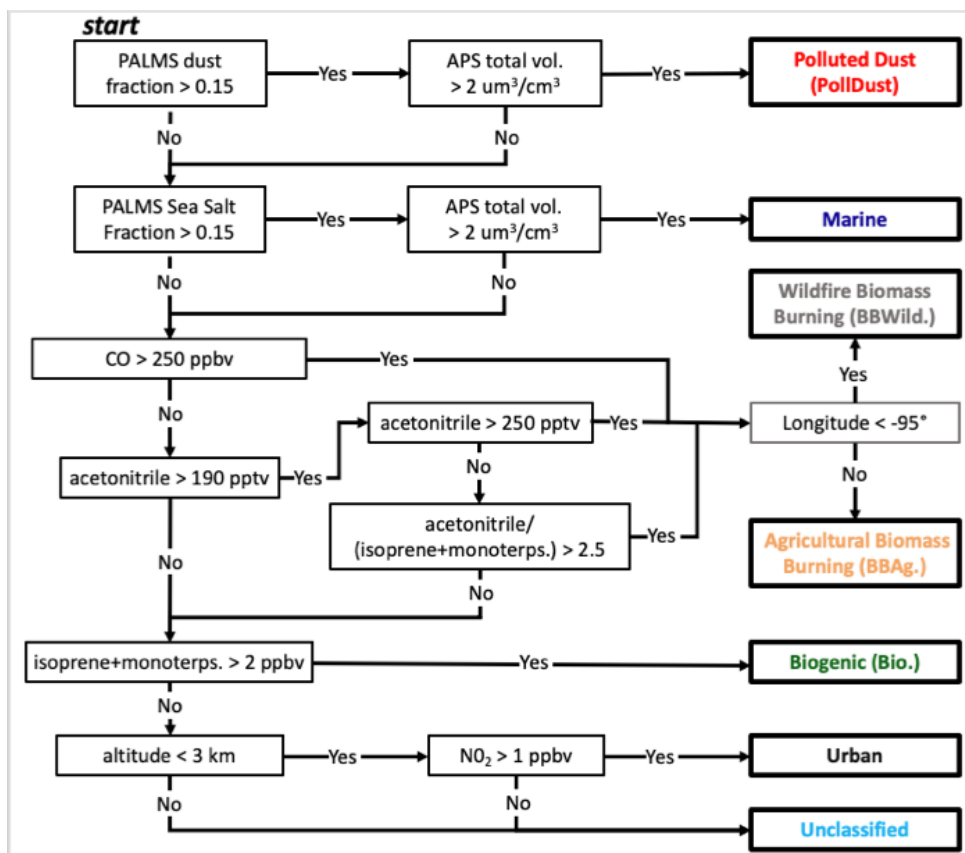


Figure 2: Scheme to pre-specify Air Mass Types (PS-AMTs; step 1 of Fig. 1) using mostly gas measurements and a method based on Espinosa et al. (2018) and Shingler et al. (2016), but modified to include Marine and two different types of BB AMTs (i.e., BBAg. and BBWild.).

3. Results

3.1 Prescribe Source-based Air Mass Types (PS-AMTs)

Figure 3 shows the PS-AMTs pre-specified using mostly measured gas phase compounds and the method described in Fig. 2.

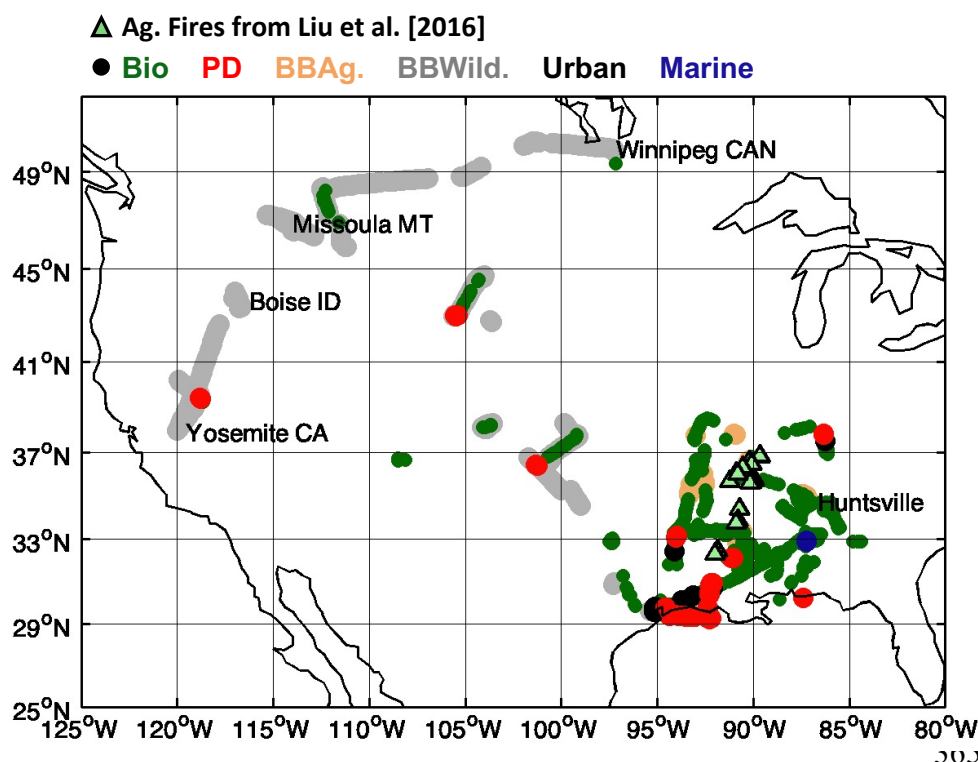


Figure 3: Air mass types pre-specified (PS-AMT) using mostly gas measurements and methods based on Espinosa et al. (2018) and Shingler et al., (2016) (see Fig. 2). The number of data points assigned to each PS-AMTs are N=31 BBAg., N=382 BBWild., N=646 Bio. and N=46 PollDust PS-AMTs. PS-AMTs Marine and Urban were not analyzed in the remainder of this study due to their limited number of data

points (N=9 Urban in black and N=7 Marine in blue). Green triangles show the location of agricultural fires according to Liu et al. (2016).

During SEAC⁴RS, according to Kim et al. (2015) and Wagner et al. (2015), the campaign-averaged aerosol mass was composed of mostly OA that is internally mixed with sulfate and nitrate at all altitudes over the SEUS i.e., 55% OA and 25% sulfate mass on average according to ground-based filter-based PM_{2.5} (Particulate Matter concentration with an aerodynamic diameter smaller than 2.5 μ m) speciation measurements from the US EPA Chemical Speciation Network. This is consistent with the findings of Edgerton et al. (2006), Hu et al. (2015), Xu et al. (2015) and Weber et al. (2007) which show that PM_{2.5} is dominated by SOA and sulfate during the summer in SEUS. Aircraft data show that 60% of the aerosol column mass (i.e., mostly OA and sulfate) is contained within the mixing layer (Kim et al., 2015). GEOS-Chem attributes OA mass as 60% from biogenic isoprene and monoterpenes sources (with a significant role of isoprene in accordance with Hu et al. (2015), Marais et al. (2016), Zhang et al. (2018), Jo et al. (2019), and Liao et al. (2015)), 30% from anthropogenic sources and 10% from open fires (Kim et al., 2015). Espinosa et al. (2018) confirm the domination of biogenic emissions in the SEUS (see their Fig. 2). Fig. 3, in agreement with these studies, shows a majority of biogenic PS-AMTs (in green, N=646), mostly in the SEUS.

During SEAC⁴RS, the air sampled by the DC8 was also affected by both long-range transport of wildfire from the west (Peterson et al., 2015; Saide et al., 2015; Forrister et al., 2015; Liu et al., 2017) and local agricultural fires mostly from the burning of rice straw along the Mississippi River Valley (Liu et al.,

2016). Fig. 3, in agreement with these studies, shows BBWild. PS-AMT in the West (in grey, N=382) and BBAG. PS-AMT in the East (in salmon, N=31). Both agricultural and wildfire smoke are mainly composed of OA, which includes a substantial amount of light-absorbing brown carbon (Liu et al., 2017), produced mostly by smoldering combustion (Reid et al., 2005; Laskin et al., 2015).

390 Although Fig. 3 also shows Urban and Marine PS-AMTs in the SEUS, these PS-AMTs were not further analyzed in the remainder of this study due to their limited number of data points (Urban in black with N=9 and Marine in blue with N=7 data points).

395 Figure 4 describes the aerosol chemical signatures of the principal PS-AMTs using the PALMS, SAGA, AMS and SP2 instruments (see line 2-5 in Table 1 for more information on these instruments and their products). Note that some aerosol components (e.g., OA, sulfate, nitrate) are very general chemical indicators and much less specific than the gas-phase chemistry they are trying to predict. These aerosol components are nonetheless directly comparable to aerosol chemical components simulated in CTMs.

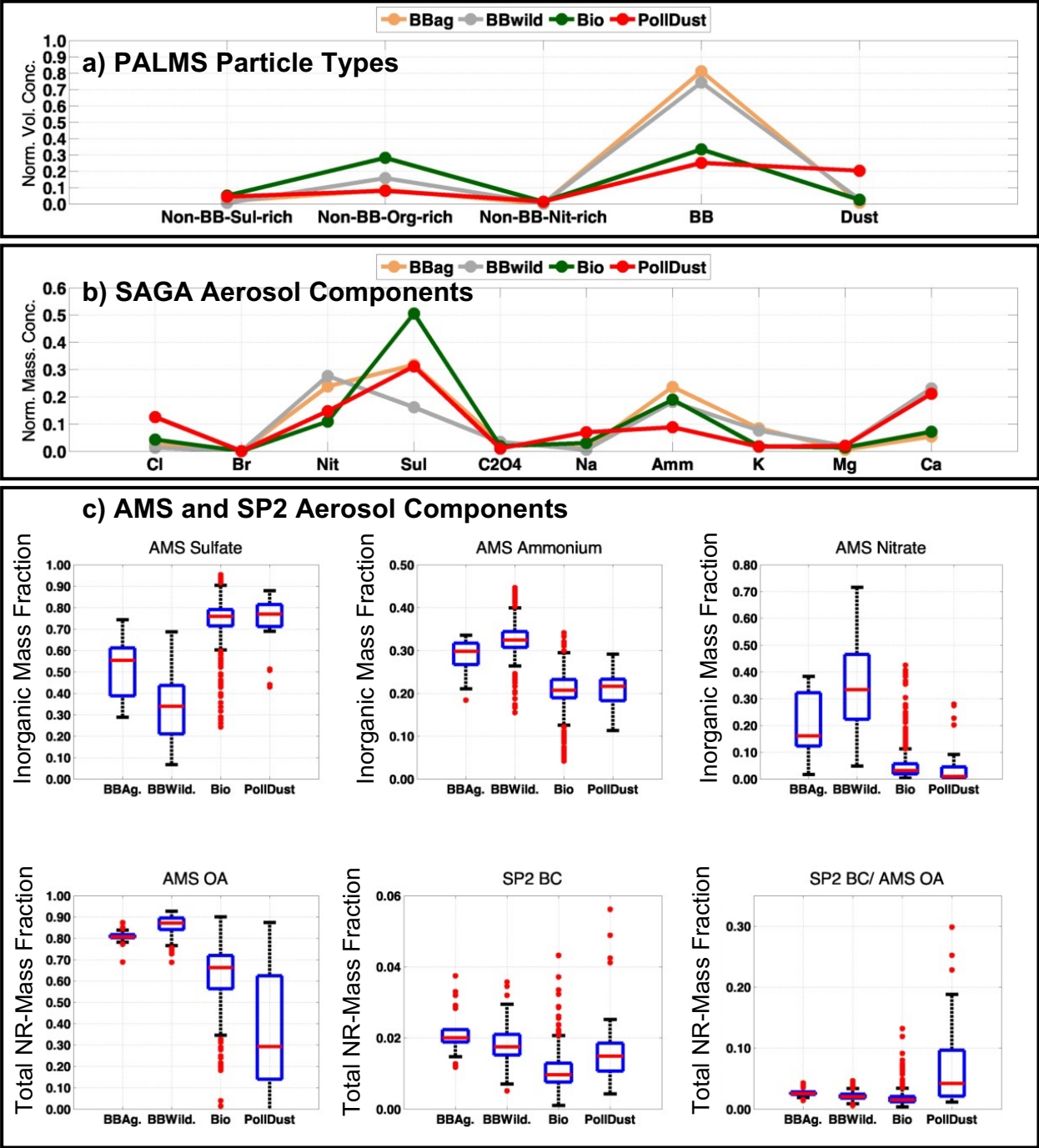


Figure 4: (a) Average PALMS normalized volume concentration per PS-AMT. PALMS normalization uses the sum of BB particles, sulfate-, organic- and nitrate-rich particles from non-BB sources, mineral dust, sulfate-organic-nitrate (SON) particles without a dominant sub-

405 component, and sea-salt (the latter two PALMS aerosol types are not shown and constitute the remainder). (b) Averaged and normalized SAGA mass concentrations per PS-AMT; normalization uses the sum of all the SAGA components in the x-axis; Cl: chloride, Br: bromide, Nit: nitrate, Sul: sulfate, C2O4: oxalate, Na: sodium, Amm: ammonium, K: potassium, Mg: magnesium and Ca: calcium (c) Normalized mass fractions of AMS sulfate, ammonium, nitrate, OA, SP2 BC and ratio of SP2 BC and AMS OA per PS-AMT. The AMS inorganic mass fraction of sulfate, ammonium and nitrate are normalized to the sum of sulfate, ammonium, and nitrate. The AMS and SP2 total Non-Refractory NR-mass fraction of OA and BC are normalized to the sum of OA, BC, sulfate, ammonium, and nitrate. In each blue box, the red horizontal line indicates the median, and the bottom and top edges of the box indicate the 25th and 75th percentiles, respectively. The black whiskers extend to the most extreme data points not considered outliers, and the outliers are plotted individually using red points. PS-AMTs Marine and Urban are not analyzed due to their limited number of data points (N=9 Urban and N=7 Marine PS-AMTs).

420 Note that the four aerosol instruments in Fig. 4 measure different aerosol properties. For instance, AMS and SAGA measure bulk concentrations of chemical sub-components (e.g., sulfate) whereas PALMS classifies individual particles into several size-resolved types, including mineral dust, BB and several non-BB types that have varying amounts of internally mixed sulfate, organic, and nitrate.

The PS-AMTs on Fig. 4 show expected chemical features:

- 425 • The BB PS-AMTs (i.e., BB_{Ag} and BB_{Wild}.) record high BB particle concentrations from PALMS in Fig. 4a, high nitrate (Nit.), ammonium (Amm.), calcium (Ca.) and potassium (K) concentrations from SAGA in Fig. 4b, high OA (i.e., >0.8) from AMS and high BC mass fractions from SP2 in Fig. 4c, in agreement with many other studies (e.g., Cubison et al., (2011); Hecobian et al., (2011); Jolleys et al., (2015), Guo et al. (2020)). The BB PS-AMTs also record higher AMS ammonium and nitrate, compared to Bio. and PollDust PS-AMTs in Fig. 4c. This is due to ammonium nitrate forming in fires by neutralization of freshly formed nitric acid from NO_x oxidation with an excess of primary ammonia (e.g., Guo et al. (2020)).
- 435 • The Bio. PS-AMTs record higher non-BB organic-rich particles from PALMS in Fig. 4a, higher SAGA sulfate concentrations in Fig. 4b, smaller nitrate and ammonium (i.e., relatively acidic) and higher sulfate particle concentrations (from e.g., coal plants) from AMS in Fig. 4c, compared to the BB PS-AMTs. As such, the Bio. PS-AMTs in this study are typical of the SEUS region (e.g., (Kim et al., 2015 and Hu 2015)). When using Positive Matrix Factorization (Ulbrich et al., 2009) on the AMS measurements, most of the organic aerosols in the Bio. PS-AMTs are composed of biogenic SOA. The Bio. PS-AMTs also record significantly lower BC concentrations from the SP2 as well as BC to OA ratios from the AMS and SP2 in Fig. 4c, compared to the BB and PollDust PS-AMTs, in accordance with e.g., Hodzic et al. (2020).
- 445 • The PollDust PS-AMTs record, as expected, high dust concentration from PALMS in Fig. 4a and high calcium (Ca) and magnesium (Mg) from SAGA in Fig. 4b. In addition, the PollDust PS-AMTs also include BB from PALMS in Fig. 4a and possibly a minor sea salt component (i.e., high sodium, Na and chloride, Cl) from SAGA in Fig. 4b as well as relatively high sulfate from SAGA and AMS in Fig. 4c. A compositional picture of the PollDust PS-AMTs from PALMS in section A.2.3 in the appendix shows

dust predominately in the coarse mode but also an accumulation mode that contains a variety of particle types, all of which contain sulfate and organic material.

450 The analysis in Fig. 4 confirms that the gas-phase-derived PS-AMTs indeed have distinct aerosol chemical properties. Therefore, we explore whether these PS-AMTs can be derived using only aerosol optical properties.

3.2 Determine Most Useful and Well Separated Aerosol Optical Properties

455 As described in section 2.2, we need to test if the PS-AMTs from section 3.1 exhibit distinct aerosol optical properties. This is an essential step to optimize the final prediction of AMTs using aerosol optical properties (DO-AMTs).

We start with the sixteen aerosol optical parameters in Table 2 (i.e., EAE, SSA, dSSA, AAE and AC at
460 different combinations of 450, 550 and 700 nm and RRI at 532 nm). Section A.2.1 in the appendix illustrates the ranges of these sixteen aerosol optical parameters, classified by PS-AMTs. Given that many of these parameters have similar properties, we select six out of these sixteen aerosol optical parameters, to simplify the analysis and presentation of results. To do that, we first look at the percentage of points unambiguously retrieved or “steady” (i.e., points that are well separated from other clusters and, hence,
465 remain in their initial clusters) when using different combinations of two out of sixteen aerosol optical parameters across all four PS-AMTs. We first select parameters AAE between 450 and 550nm and RRI at 532nm as they form the only combination of two parameters to achieve >65% “steady points” for all four PS-AMTs (see Fig. A5 in the appendix). The rest of the six optical parameters are either chosen at 550nm (i.e., closest wavelength to 532 nm) or between 450 and 550nm. As a result, the six parameters
470 we choose for the remainder of this study are dSSA 450-550 nm, RRI 532 nm, EAE 450-550 nm, AAE 450-550 nm, SSA 550 nm and AC at 550nm. Among these parameters, the usefulness of parameters dSSA 450-550 nm, EAE 450-550 nm, SSA 550 nm and AC at 550nm only becomes apparent in a 3-D parameter space (see Fig. A6 and its orange boxes in the appendix, which record >65% “steady points” for many combinations of three parameters among these six selected aerosol optical parameters).

475 Figure 5 illustrates the range of these six aerosol optical properties for each PS-AMT. Fine particles (i.e., BBWild., BBAG. and Bio. PS-AMTs with higher EAE values) show mostly well-separated variability in RRI, AAE and dSSA. Coarse particles (i.e., PollDust PS-AMT with lower EAE values) are optically distinctive from the other PS-AMTs, particularly showing lower RRI, higher AAE and higher dSSA. In
480 agreement with Selimovic et al. (2019; 2020) in Missoula, MT, we seem to also observe separate optical signatures, and more specifically different AAE ranges, for BBAG. and BBWild. PS-AMTs during SEAC⁴RS.

The aerosol optical properties of the PollDust PS-AMTs in this study differ from the ones of the “pure dust” AMT in Russel et al. (2014). The “pure dust” in Russel et al. (2014) is based on AERONET
485 measurements in various dusty regions of the world. In this study, PollDust PS-AMT show a median EAE of ~1.3 between 450 and 550 nm and a median RRI of ~1.4 at 532 nm on Fig. 5, compared to respectively

~0 between 491 and 864 nm and 1.53 at 670 nm for AERONET-based “pure dust” in Russel et al. (2014). We show that the higher PollDust PS-AMT EAE values in our study are due to the presence of accumulation mode non-dust aerosols, which constitute a significant contribution to the total number and volume concentration of particles (see Fig. A7 in the appendix for a compositional picture of PollDust PS-AMT). Similarly, we also suggest that the low PollDust PS-AMT RRI values are due to its non-dust accumulation mode, which is generally more hygroscopic than pure dust and may have a larger contribution to the PollDust total Growth Factor. We refer the reader to Fig. A4 in the appendix for a closer look at RRI values in the case of PollDust PS-AMTs from the PI-Neph and DASH-SP instruments separately.

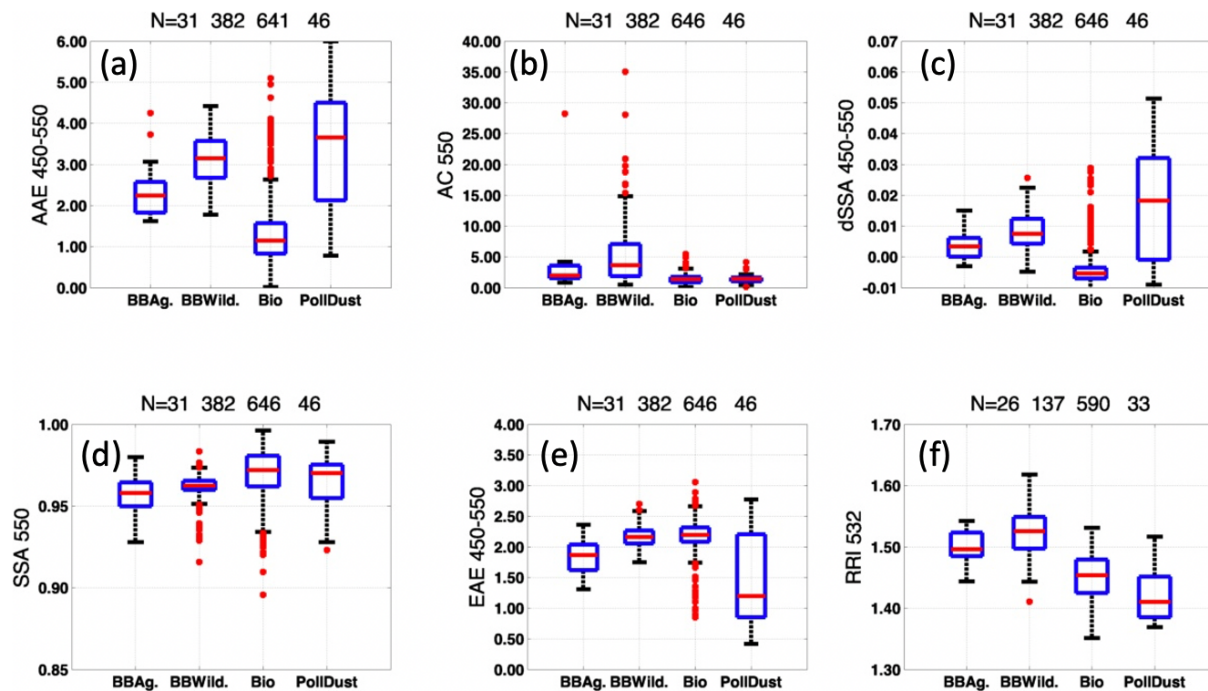


Figure 5: Optical characterization of PS-AMTs using the LARGE, PI-Neph and DASH-SP instruments (see Table 1). In each blue box, the red horizontal line indicates the median, and the bottom and top edges of the box indicate the 25th and 75th percentiles, respectively. The black whiskers extend to the most extreme data points not considered outliers, and the outliers are plotted individually using red points. (a) AAE: Absorption Angstrom Exponent, (b) AC: Absorption Coefficient, (c) dSSA: difference in Single Scattering Albedo, (d) SSA: Single Scattering Albedo, (e) EAE: Extinction Angstrom Exponent, (f) RRI: Real Refractive Index. Numbers in the title correspond to the number of points behind each box-whisker for the respective BBAg., BBWild., Bio. and PollDust PS-AMTs.

Figure 6 shows “steady” values (i.e., fraction of cases of a given type that are correctly identified) for combinations of two, three and four optical parameters out of the six selected aerosol optical parameters in Fig. 5 and four AMTs (i.e., BBAg., BBWild., Bio. and PollDust). Moving forward, we select the sixteen combinations of optical parameters highlighted by grey boxes and black dots in Fig. 6, as they show > 65% “steady points” for PS-AMTs BBAg., BBWild., Bio. and PollDust. These combinations are numbered in grey at the top of Fig. 6.

515

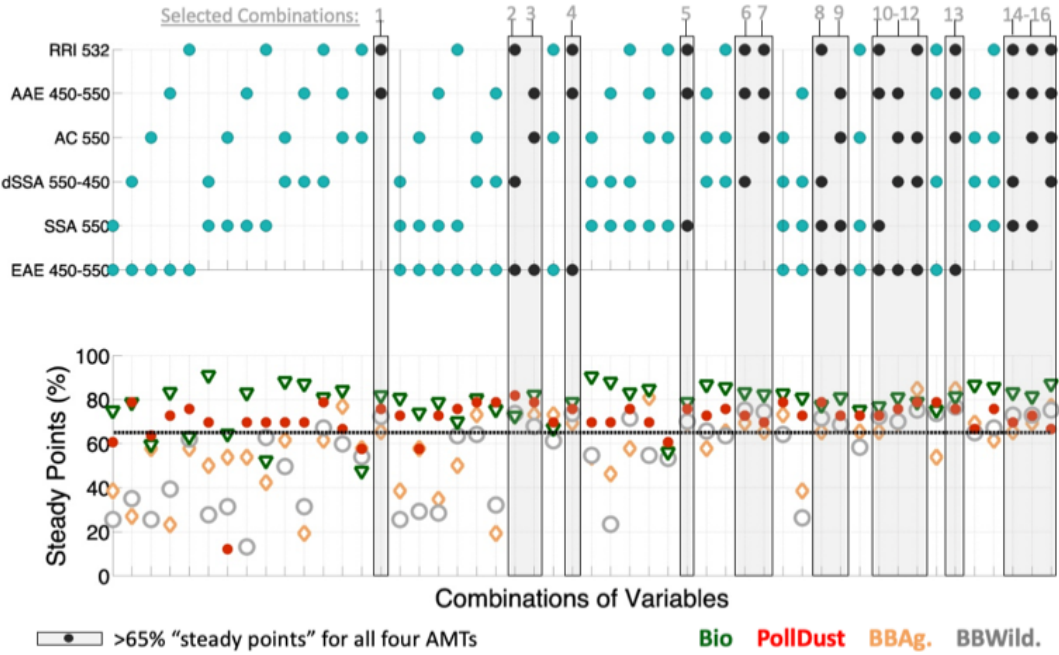


Figure 6: Percentage of “steady” points (i.e., fraction of cases of a given type that are correctly identified) in the lower panel when using different combinations of aerosol parameters in the upper

535 **panel for each PS-AMT. Grey boxes and black points depict combinations of optical parameters showing > 65% “steady points” for PS-AMTs BBAg., BBWild., Bio. and PollDust. RRI: Real Refractive Index, AAE: Absorption Angstrom Exponent, AC: Absorption Coefficient, dSSA: difference in Single Scattering Albedo, SSA: Single Scattering Albedo, EAE: Extinction Angstrom Exponent**

540

Let us note that for some cases, the fraction of “steady” points seems to decrease when adding classifying variables. These cases were investigated and are mostly due to fewer data points that are non-“steady” when adding classifying parameters, out of an already small total number of datapoints (e.g., a combination of EAE, dSSA, AAE and RRI show <65% “steady points” for BBAg. PS-AMT, compared to >65% “steady points” for a combination of EAE, AAE and RRI; this is due to 4 more “steady” points (N=18) when using a combination of 3 parameters, compared to 4 parameters (N=14), out of a total of N=26 cases).

550 Moreover, we suggest that higher aerosol loadings within the air masses allow for more accurate identification by optical properties, due to higher accuracy of the aerosol optical properties themselves.

For example, we have seen an increase from ~80% to 100% “steady” data points in the BBWild. PS-AMT when using EAE, AAE and RRI when extinction coefficients increased from 30-40 Mm⁻¹ to 60-70 Mm⁻¹ (number of data points between N=11 and N=20).

555 **3.3 Define Optical-based Class Definitions and Derive Optical-based Air Mass Types (DO-Class and DO-AMTs)**

Next, we derive AMTs (DO-AMTs), followed by a comparison between DO-AMTs and the initial PS-AMTs to test the ability of aerosol optical properties alone to capture PS-AMTs.

560 As described in section 2.2, to derive DO-AMTs using the SCMC method, we need (i) a combination of useful and well separated optical properties (e.g., EAE, AAE and RRI or combination #4 in Fig. 6), (ii) a set of defined classes of reference (i.e., a training dataset that we call DO-Class) and (iii) the computation of the Mahalanobis distance between each observation we want to classify in a test data set and each of the clusters from the training dataset.

565 We introduce Table 3, which records the number of data points behind each step in our study.

Number of Data		BBAg.	BBWild.	Bio.	PollDust	Total	Major Steps (see Fig. 1)
1	PS-AMTs	31	382	646	46	1105	(1) Pre-specify Source-based PS-AMTs (see colored points in Fig. 3)
2	Valid AAE (Fig. 5a)	31	382	641	46	1100	(2) Determine most useful and well separated aerosol optical properties
3	Valid RRI (Fig. 5f)	26	137	590	33	786	
4	Valid EAE, AAE and RRI Observations (#4 in Fig. 6)	26	137	585	33	781	
5	"Steady" points (*)	18	101	460	25	604	
6	To define DO-Class	391					(3) Define optical-based Classes, DO-Class; use "steady" portion of first ~half of observations
7	DO-Class (*)	8	52	238	13	311	

8	To derive DO-AMTs	389					(4) Derive optical-based AMTs, DO-AMTs; apply SCMC method, using DO-Class, on second ~half of observations
9	Known DO-AMTs (*)	32	55	217	77	381	
10	Unknown DO-AMTs (*)	8					
11	PS-AMTs from dataset in 18	13	68	292	16	389	(5) Compare DO-AMTs and PS-AMTs
12	DO-AMTs similar to PS-AMTs (*)	10	54	213	13	290	
13	DO-AMTs similar to PS-AMTs as a % of assigned DO-AMTs (19) (*)	31	98	98	17	-	
14	DO-AMTs similar to PS-AMTs as a % of PS-AMTs (111) (*)	77	79	73	81	-	
(*) in the case of combination #4 in Fig. 6 i.e., EAE, AAE and RRI							

570 **Table 3: Number of data points per AMTs behind each step in our study. PS-AMTs Marine and Urban are not analyzed due to their limited number of data points (N=9 Urban and N=7 Marine PS-AMTs). EAE: Extinction Angstrom Exponent, AAE: Aerosol Absorption Exponent and RRI: Real Refractive Index.**

575 The first line of Table 3 shows the number of data points per PS-AMTs (see Fig. 3). Then, line 2, 3 and 4 of Table 3 show the valid number of AAE, RRI and a combination of EAE, AAE and RRI data points. Line 5 of Table 3 shows the “steady” number of data points per PS-AMT in the case of a combination of EAE, AAE and RRI (see Fig. 6). To create the training dataset DO-Class (line 7 in Table 3), we select the “steady” portion of half (every other sample) of the entire set of valid datapoints (line 6 in Table 3).
580 The test data set that we want to classify as DO-AMTs is the other half of the entire set of valid datapoints (line 8 in Table 3). This DO-AMT dataset is made of “steady” and non- “steady” data points.

Figure 7 illustrates the separability of the DO-Class in the 3-D space made of aerosol optical parameters EAE, AAE and RRI. The regions of the DO-Class are described by colored ellipses representing the mean, variance, and covariance of the DO-Class training set. It also shows that most of the DO-Class represent the original source-based PS-AMTs (represented by colored triangles on Fig. 7). However, let us note
585 that a distinct portion of the Bio. PS-AMTs (green triangles) seem to not be represented by the Bio. DO-

Class (green ellipse). These Bio. PS-AMTs show higher AAE and lower EAE values and mostly fall into the PollDust DO-Class instead (red ellipse).

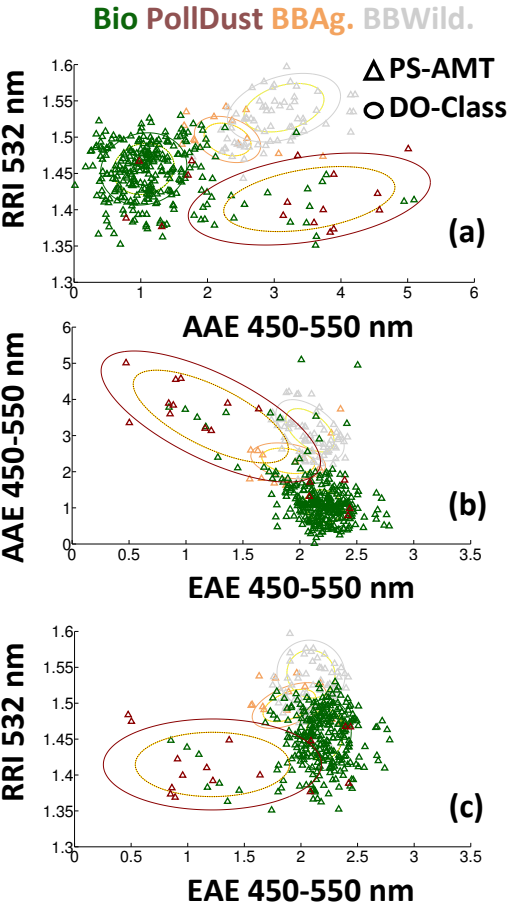


Figure 7: DO-Class definition (solid and dashed ellipses colored by AMTs defining boundaries of the DO-Class clusters; DO-Class data points are not plotted) and prescribed source-based PS-AMTs (triangles colored by AMTs). 75% of the DO-Class are contained in the solid ellipses and 50% of the DO-Class are contained in the dashed ellipses. RRI: Real Refractive Index, AAE: Absorption Angstrom Exponent, EAE: Extinction Angstrom Exponent. Graphs (a), (b) and (c) illustrate PS-AMT and DO-Class in the respective 2-D spaces made of AAE-RRI, EAE-AAE and EAE-RRI.

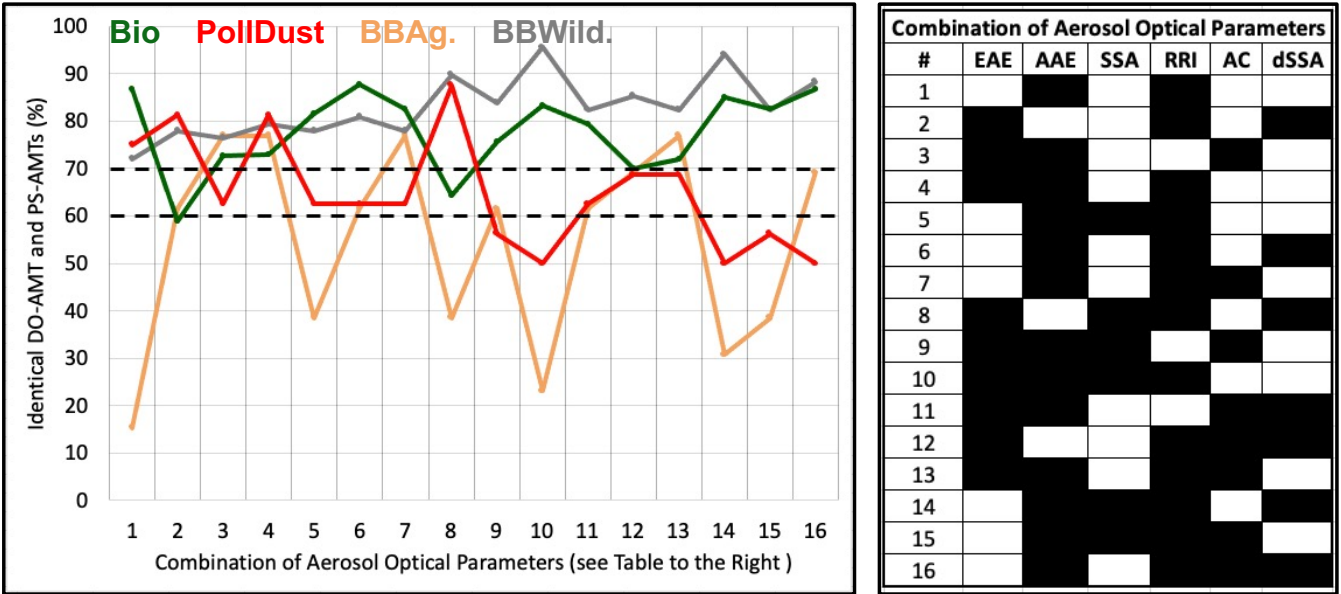
Line 9 in Table 3 shows the number of DO-AMTs (correctly and incorrectly) classified as BBAg., BBWild., Bio. or PollDust AMTs using the combination of EAE, AAE and RRI as an example, the SCMC method and the DO-Class reference clusters. Most points from the test data set were assigned an AMT (see N=381 assigned DO-AMTs on line 9, compared to N=8 unknown on line 10 of Table 3). Unclassified/unknown DO-AMTs are those where the 3-D data point is outside the 99% probability surface for all four DO-Classes.

3.4 Compare Optical-based and Source-based Air Mass Types (DO- vs. PS-AMTs)

Once we have derived DO-AMTs from optical properties (i.e., inferred our wolf based on its tracks in Fig. 1), we need to assess how many of the DO-AMTs agree with those originally assigned as PS-AMTs. Line 11 in Table 3 shows the number of prescribed PS-AMTs in each category when only looking at the test dataset to derive DO-AMTs on line 8 of Table 3 (N=389). Line 12 in Table 3 shows the number of DO-AMTs that are identical to PS-AMTs. Line 13 and 14 show the same result, but as a percentage of the respectively derived DO-AMTs or prescribed PS-AMTs in the same category. In Table 3, we find 77% BBAg., 79% BBWild., 73% Bio. and 81% PollDust PS-AMTs are correctly reflected in the DO-AMTs. This result can also be seen for combination #4 in Fig. 8 (i.e., EAE, AAE and RRI).

Fig. 8 illustrates the percentage of identical DO-AMTs to PS-AMTs when using each of the sixteen combinations of optical parameters illustrated by black squares in the table of Fig. 8. These combinations are the same as the ones in grey at the top of Fig. 6. This percentage, like line 14 in Table 3, is computed

as the number of DO-AMTs that agree with those originally assigned as PS-AMTs, compared to the total number of prescribed PS-AMTs in each category in our test dataset (e.g., line 11 in Table 3).



630 **Figure 8: Identical DO-AMT and PS-AMTs as a percentage of prescribed PS-AMTs in each**
category when using the different combinations of optical parameter listed in the table to the right
(bold squares show combination on each line) and for the four PS-AMTs BBAg. (salmon),
BBWild. (grey), Bio. (green) and PollDust (red). Bold horizontal dashed lines show 60% and 70%
identical DO-AMT and PS-AMTs.

635 According to Fig. 8, the entire sixteen combinations of aerosol optical properties listed in the Table of
Fig. 8 as bold squares seem to capture both the Bio. and BBWild. PS-AMTs (>~60% identical DO-AMT
and PS-AMTs in green and grey solid lines in Fig. 8). We remind the reader that these PS-AMTs are
mostly based on gas measurements (see Fig. 2) and are dominated by different aerosol species (see Fig.
640 4).

On the other hand, fewer combinations of aerosol optical parameters seem to adequately capture the
BBAg. and PollDust PS-AMTs. Further analysis shows that, in average, most DO-AMTs assigned to the
BBAg. and PollDust categories are, in fact, misclassified and failing to capture the Bio. PS-AMTs. As
shown earlier in Fig. 7, we suggest these DO-AMTs fail to capture the Bio. PS-AMTs because the Bio.
645 DO-Class might not be entirely representative of the Bio. PS-AMTs (see green triangles outside of the
green ellipses in Fig. 7).

Note that three combinations of aerosol optical parameters, namely #4 (EAE, AAE and RRI), #12 (EAE,
RRI, AC and dSSA) and #13 (EAE, AAE, RRI and AC) in Fig. 8, seem to capture all four PS-AMTs
particularly well (>~70% identical DO-AMT and PS-AMTs). Let us mention that results linked to the use

650 of the absorption coefficient, AC, an extensive property that is dependent on aerosol loading, is likely to be unique to this study and might not be representative of any other field campaign.

4. Conclusion

655 One desire of our scientific community is to ultimately translate the space-based “total atmospheric column effective” AMTs such as biomass burning, dust, urban industrial, and polluted marine into chemical species with defined emission source inventories and formation/aging chemistry such as sulfate, BC, OA, SOA, nitrate, dust, or sea salt to better improve models. Fully achieving that goal might not be feasible and progress can only be incremental. This study constitutes a first step towards the goal of translating the space-based “total atmospheric column effective” aerosol optical properties and derived optical-based AMTs into source-based AMTs.

660 Current satellite derived AMTs inferred by various techniques are useful to provide spatial context to support other observations of aerosols and clouds or evaluate other aerosol type classifications. However, these satellite derived AMTs are ambiguously defined and might often be misclassified.

665 The AMTs in this study are defined, characterized, and derived using gas-phase, chemical and optical instruments on the same aircraft. This reduces errors in measurements/retrievals, due to spatio-temporal colocation and ambiguities in the selection of the AMT training dataset. We also specifically investigate the strengths and weaknesses of various aerosol optical properties used as tools to define AMTs and how much these optical properties can capture dominant aerosol speciation.

670 We first define AMTs using mostly airborne gas-phase measurements during SEAC⁴RS. We find distinct optical signatures for biomass burning (from agricultural/ prescribed or wildfires), biogenic and dust-influence AMTs (Marine and Urban AMTs show too few data points to analyze). Useful aerosol optical properties to characterize these signatures are the extinction angstrom exponent between 450-550nm, the single scattering albedo at 550nm, the difference of single scattering albedo in two wavelengths between 450-550nm, the absorption coefficient at 550nm, the absorption angstrom exponent between 450-550nm, and the real part of the refractive index at 532nm. We then use these aerosol optical properties, prescribe a well-separated AMT training dataset, and use the pre-specified clustering and Mahalanobis classification method to derive optical-based AMTs during SEAC⁴RS. We find that by using any of sixteen combinations of these six optical parameters, over 65% of optical-based wildfire biomass burning and biogenic AMTs agree with their source-based analogue. We find that biogenic, BB from wildfires, BB from agricultural fires, and polluted dust AMTs, when prescribed using mostly airborne *in situ* gas measurements, can be successfully extracted from at least three combinations of airborne *in situ* aerosol optical properties over the US during SEAC⁴RS, such that more than 70% of optical observations are typed consistently with source-based analog. However, we find that misclassifications are not evenly distributed across the classes, and specifically the optically based classifications for BB from agricultural fires and polluted dust include a large percentage of misclassifications that limit the usefulness of results relating to those classes.

690 5. Discussion

We suggest a similar study should be performed using data from additional airborne field campaigns which have the necessary, or equivalent, gas-phase measurements to derive source based-AMTs and many of the critical optical properties to extract optical based-AMTs. First, this would provide more robust statistics e.g., particular attention should be given to revisit the BB from agricultural fires and polluted
695 dust AMTs in this study. Second, this would provide more AMTs/sub-AMTs to analyze e.g., Urban and Marine AMTs should be visited during CAMP²EX (Clouds, Aerosol and Monsoon Processes-Philippines Experiment) or KORUS-AQ (An International Cooperative Air Quality Field Study in Korea) and other types of BB and at different aging stages should be visited during FIREX-AQ (Fire Influence on Regional to Global Environments and Air Quality). Finally, this would also help assess if these chemical and optical
700 signatures are reproducible from one year to another.

In this study, we obtained *in situ* aerosol optical signatures. Another essential step should be to examine optical signatures from space-based passive remote sensor(s), which derive total column effective ambient aerosol optical properties (instead of properties measured at the altitude of the aircraft in this
705 study). One way to answer this question would be to compare the defined optical-based classes (DO-Class) signatures using collocated airborne *in situ* aerosol optical properties and total column aerosol optical properties measured or inferred by sunphotometry (e.g., airborne 4STAR, Spectrometers for Sky-Scanning Sun-Tracking Atmospheric Research (Dunagan et al., 2013) or ground-based AERONET). This DO-Class database could then be used as an optical-based training dataset to enable widespread derivation
710 of optical-based AMTs (DO-AMTs) using existing and future orbital and suborbital remote sensing instruments and networks.

The space mission addressing the designated observable Aerosol, Cloud, Convection and Precipitation (ACCP) from the NASA decadal survey (National Academies
715 of Sciences, Engineering, and Medicine, 2018) is currently designing its suborbital (airborne and ground-based) component to address science questions that cannot be addressed from space (e.g., bridging satellite-inferred aerosol optical properties and aerosol speciation). This study illustrates how essential it is to explore existing airborne datasets to bridge chemical and optical signatures of different AMTs, before the implementation of future spaceborne missions and their corresponding suborbital field campaign(s)
720 (e.g., upcoming spaceborne polarimeters SPEXone (Hasekamp et al., 2019) and Hyper-Angular Rainbow Polarimeter HARP-2 onboard the NASA Plankton, Aerosol, Cloud, ocean Ecosystem (PACE) (Werdell et al., 2019) and the multi-viewing multi-channel multi-polarization imager (3MI) (Fougnie et al., 2018) to be launched in the next 3 years or the next generation of Earth Observing System (EOS) satellites addressing NASA's ACCP).

725 Most of the six optical properties in this study (i.e., extinction angstrom exponent, single scattering albedo, difference of single scattering albedo, absorption coefficient, absorption angstrom exponent, and

real part of the refractive index) are routinely derived by *in situ* and remote sensing instrumentation/networks (see Table 4). Some optical properties are more likely to present a higher uncertainty when measured from suborbital field campaigns and/ or from satellites. The real part of the refractive index, for example, although generally more uncertain, is highly desirable in many combinations of optical parameter to capture both the BB from wildfires and biogenic AMTs in this study. We strongly suggest future airborne campaigns consider including *in situ* measurements of AAE and RRI (very few of the campaigns to date flew PI-Neph and/or DASH-SP instruments) and a special attention should be given to deriving these parameters accurately from space. Our analysis has the advantage of providing alternate combinations of optical parameters when one optical parameter is either not available or too uncertain.

Aerosol Optical Parameter	Routinely Observed from Aircraft	Routinely Observed from Satellites	Importance in this study
Extinction Angstrom Exponent, EAE	High	High	High
Single Scattering Albedo, SSA	Medium	Medium	High
Difference in SSA, dSSA	Medium	Medium	High
Absorption Coefficient, AC	Medium	Low	High
Aerosol Absorption Exponent, AAE	Medium	Medium	High
Real Refractive Index, RRI	Low	Low	High

Table 4: Frequency at which the six aerosol optical parameters in our study are routinely derived from aircraft and current passive satellite sensors and importance of these optical parameters in our study. RRI: Real Refractive Index, AAE: Absorption Angstrom Exponent, AC: Absorption Coefficient, dSSA: difference in Single Scattering Albedo, SSA: Single Scattering Albedo, EAE: Extinction Angstrom Exponent

Ultimately, this technique and its results has the potential to provide a much broader observational aerosol data set to evaluate global transport models than is currently available. Current satellite derived AMTs seem to marginally help models. One way to assess models would be to directly compare satellite derived AMTs to AMTs derived from modeled optical properties (which are, in turn, computed from modeled chemical composition) using the same classification method (e.g., Taylor et al., 2015, Dawson et al. (2017), Nowottnick et al. (2015), Meskhidze et al. (2021)). However, it would be difficult to define the main source of errors in the case of a disagreement between model- and observation-based AMTs. Potential causes of such a disagreement could be a combination of observation and method-specific errors or model-specific errors (e.g., the assumed model size distribution, dry refractive index, growth factor per

755 specie, mass extinction efficiency per species, estimated mass per species, RH, transport, chemical
processing, emissions, and other physiochemical variables). Let us emphasize that the technique and
results in this study, alone, will not be able to fully explain any discrepancies between model and
observations. However, we suggest that the use of near-simultaneous gas-phase, chemical and optical
760 based AMTs to mostly model-specific errors. Moreover, as the AMTs in this study are less ambiguously
defined (e.g., to each AMT corresponds an averaged distribution of aerosol chemical composition), we
suggest that this may allow the assessment (and, by extension, improvement) of a few aerosol processes
simulated in CTMs.

765 **Appendix A**

A.1 Additional Information on Methods

A.1.1 Method to Cloud-screen, Filter, and Humidify Airborne Observations

This section describes the cloud-screening, filtering, humidification, and colocation involved in the
computation of the final set of sixteen optical parameters (i.e., EAE, dSSA and AAE between 450-550,
770 550-700 and 450-700 nm, AC, SSA at 450, 550 and 700nm and the RRI at 532 nm) in this study.

The **LARGE TSI nephelometer and PSAP instruments** operate under dry conditions. The only
measurement provided at ambient conditions is the EC at 532nm. In this work, we need LARGE EC and
SC at 450, 550 and 700nm at ambient conditions. To do that, we use the parameter “fRH550_RH20to80”
775 at 550 nm provided by the LARGE f(RH) system (different from the TSI or PSAP instruments) and an
exponential curve to obtain the impact of hygroscopic growth on the aerosol light scattering coefficient
i.e., the scattering enhancement factor f(RH) at 450, 550 and 700 nm. Ambient SC at 550 nm, for example,
is computed as the product of dry SC at 550 nm and f(RH) at 550nm. We filter out any values of LARGE
dry SC at 450 nm $\leq 10 \text{ Mm}^{-1}$ and LARGE ambient SSAC at 863 nm ≤ 0.7 .

780 **DASH-SP** provides measurements of $\text{RRI}_{\text{DASH-SP_dry}}$, information on the particle hygroscopicity, $\kappa_{\text{DASH-SP_dry}}$,
and the particle diameter, $\text{Dp}_{\text{DASH-SP_dry}}$, in dry conditions. We compute DASH-SP RRI in ambient
conditions, $\text{RRI}_{\text{DASH-SP_ambient}}$, using $\text{RRI}_{\text{DASH-SP_dry}}$, $\kappa_{\text{DASH-SP_dry}}$, and the ambient relative humidity and
temperature measurements, RH_{HSP} and T_{HSP} , provided by the AIMMS-20 (Aircraft-Integrated
785 Meteorological Measurement System) or 3D-winds instruments. First, we vary the Growth Factor, GF_{var} ,
from 1.02 to 1.5 by increments of 0.01 and compute the particle hygroscopicity, κ_{var} , for given
 RH_{HSP} , T_{HSP} and $\text{Dp}_{\text{DASH-SP_dry}}$ measurements as follows:

$$\kappa_{\text{var}} = (\text{GF}_{\text{var}}^3 - 1) \times (1 - \kappa_a) / \kappa_a \quad (\text{Eq. A.1.1a})$$

Where:

- 790
- $\kappa_a = (\text{RH}_{\text{HSP}} / 100\%) / \exp(\text{C}_{\text{amb}} / (\text{GF}_{\text{var}} \times \text{Dp}_{\text{DASH-SP_dry}}))$
 - $\text{C}_{\text{amb}} = (4 \times \sigma_{\text{sa}} \times \text{M}_w) / (\text{R} \times \text{T}_{\text{HSP}} \times \rho_w)$

- $\sigma_{sa} = 0.0761 - 1.55 \times 10^{-4} \times (T_{HSKP} - 273)$;
- $M_w = 18.01528/1000$ kg/mole
- $R = 8.3144598$
- $\rho_w = 1000$ kg/m³

795

We select the growth factor, GF_{var} , that provides the closest κ_{var} value to the $\kappa_{DASH-SP_dry}$ measurement. We call this growth factor GF_{select} . Finally, we compute the ambient RRI, $RRI_{DASH-SP_ambient}$, using $RRI_{DASH-SP_dry}$ and GF_{select} obtained in the previous steps and equation 5 of Mallet et al. (2003) (based on Hänel (1976)) as follows:

800

$$RRI_{DASH-SP_ambient} = RRI_w + (RRI_{DASH-SP_dry} - RRI_w) \times (GF_{select})^{-3} \quad (\text{Eq. A.1.1b})$$

Where $RRI_w = 1.33$. Let us note that Aldhaif et al. (2018) demonstrate the limitations of using the volume-weighted mixing rule approach above, especially in the presence of OA.

805

The PI-Neph provides measurements of dry phase function (P_{11}) and the second element of the scattering phase matrix (P_{12}) at three wavelengths over an angular range spanning $>170^\circ$. These measurements are fed into the GRASP (Dubovik et al., 2014) algorithm to obtain retrieved values of spectral complex refractive index, a parameterized size distribution as well as derived optical properties like scattering coefficients. In this work we utilize these optical properties provided by PI-Neph in dry conditions: the SC at 532 nm, $SC_{PI-Neph_dry}$, the dry size distribution, $dNdlr_{PI-Neph_dry}$ and the Refractive Index, $RI_{PI-Neph_dry}$. First, we compute the “target” ambient SC at 532 nm, $SC_{PI-Neph_target}$, as the product of $SC_{PI-Neph_dry}$ and LARGE $f(RH)$ measurements at 550nm. Second, we compute the ambient SC at 532 nm, $SC_{PI-Neph_ambient}$, corresponding to each GF_{var} from 1 to 1.5 by increments of 0.01 using (i) a Mie code (Mishchenko et al., 2002) and, as input to the Mie code, (ii) the ambient size distribution and corresponding radii, computed from $dNdlr_{PI-Neph_dry}$ and GF_{var} , (iii) the ambient refractive index computed from $RI_{PI-Neph_dry}$ and GF_{var} (see Eq. A.1.1b) and a prescribed geometric standard deviation (i.e., ~ 1.12 , which results in similar computed and provided $SC_{PI-Neph_dry}$ values when using the same Mie code and initial parameters $dNdlr_{PI-Neph_dry}$ and $RI_{PI-Neph_dry}$). Third, we select GF_{var} (we call this growth factor, GF_{select}) and corresponding $RRI_{PI-Neph_ambient}$ that records the minimum difference between $SC_{PI-Neph_ambient}$ and $SC_{PI-Neph_target}$.

810

815

820

We compute ambient **AMS and SP2** mass concentrations using the parameter “stdPT-to-AMB_Conversion_AMS-60s” reported with the AMS data. SP2 BC standard concentration (referred to as “refractory black carbon”, and experimentally equivalent to elemental carbon at the 15% level (Petzold et al., 2013; Kondo et al., 2011; Perring et al., 2017)), originally in $ng.m^{-3}$, is converted into $\mu g.m^{-3}$ and scaled upwards, on a flight-by-flight basis, to represent the entire accumulation mode (on average by 1.14). The AMS sulfate, ammonium and nitrate are normalized to the sum of sulfate, ammonium, and nitrate. The AMS OA and SP2 BC are normalized to the sum of OA, BC, sulfate, ammonium, and nitrate. In the case of **SAGA**, bromide and chloride are set to zero if under the detection limit of 0.0107 and 0.0391 $\mu g.m^{-3}$. In the case of **PALMS**, we use volume weighted products (Froyd et al., 2019). In this study, PALMS particle classes include mineral dust, sea salt, biomass burning, and sulfate-organic-nitrate mixtures (SON). The SON class was further refined into organic-rich, sulfate-rich, and nitrate-rich particle types, plus a remainder of SON particles that did not exhibit a dominant chemical sub-component. To define the Marine and Polluted Dust AMTs, PALMS composition was combined with aerosol size

825

830

835 distribution data from LARGE to yield integrated volume fractions of mineral dust and sea-salt particle types from $D=0.1-5\ \mu\text{m}$ based on the method of Froyd et al. (2019). The average AMT chemical composition is determined as a raw number fraction of particles observed by PALMS.

A.1.2 Method to Collocate Airborne Observations

840 All the airborne observations are cloud screened using wing-mounted cloud probes. Table A1 defines three datasets used in this study with its associated number of data points, called AIRBO₁, AIRBO₂ and AIRBO₃ and their combination, AIRBO. In all four datasets, the LARGE data is first collocated to housekeeping (HSKP) data (i.e., select same “start_utc” in seconds) and humidified/ filtered (see A.1.1).

845 In the AIRBO₁ dataset, we compute the mean HSKP and LARGE values in a ± 30 second range centered on each collocated AMS-PALMS-SP2 “start_time” (i.e., the 1 min “merged” file). We then record LARGE averaged values if (i) the average is made of at least 20 points and (ii) the standard deviation of the LARGE EAE is below 30%. In the AIRBO₂ dataset, we compute the mean HSKP and LARGE values between each DASH-SP “start_utc” and “end_utc”. We record HSKP, humidified LARGE and DASH-SP values if the following four parameters are below 30%: (i) the standard deviation of the LARGE EAE, 850 (ii) the difference between $\kappa_{\text{DASH-SP_dry}}$ and κ_{var} (Eq. A.1.1a), (iii) the standard deviation of RH_{HSKP} and (iv) the standard deviation of T_{HSKP} . In the AIRBO₃ dataset, we compute the mean HSKP and LARGE values between each PI-Neph “start_utc” and “end_utc”. We record HSKP, humidified LARGE and PI-Neph values if the following four parameters are below 30%: (i) the standard deviation of the LARGE EAE, (ii) the standard deviation on $\text{scat}_{\text{PI-Neph_dry}}$, (iii) the standard deviation on LARGE $f(\text{RH})$, and the 855 difference between PI-Neph $\text{SC}_{\text{PI-Neph_target}}$ and $\text{SC}_{\text{PI-Neph_ambient}}$ (see A.1.1). Finally, we collocate the HSKP-LARGE-DASH-SP (HSKP-LARGE-PI-Neph) to the AMS-PALMS-SP2 datasets in the case of AIRBO₂ (AIRBO₃). To do that, if there are multiple AMS-PALMS-SP2 data points between each HSKP-LARGE-DASH-SP (HSKP-LARGE-PI-Neph) averaged time stamp, we average all AMS-PALMS-SP2 data between the HSKP-LARGE-DASH-SP (HSKP-LARGE-PI-Neph) averaged time stamps. If there 860 are no multiple AMS-PALMS-SP2 data points between the HSKP-LARGE-DASH-SP (HSKP-LARGE-PI-Neph) averaged time stamps, we select the closest AMS-PALMS-SP2 data in time to the HSKP-LARGE-DASH-SP (HSKP-LARGE-PI-Neph) averaged time stamps. The dataset in this study, AIRBO, was obtained by first, selecting common 1 min UTC time stamps from all 3 datasets, and then arbitrarily selecting, in order of priority when present, AIRBO₂, AIRBO₁ and AIRBO₃.

865

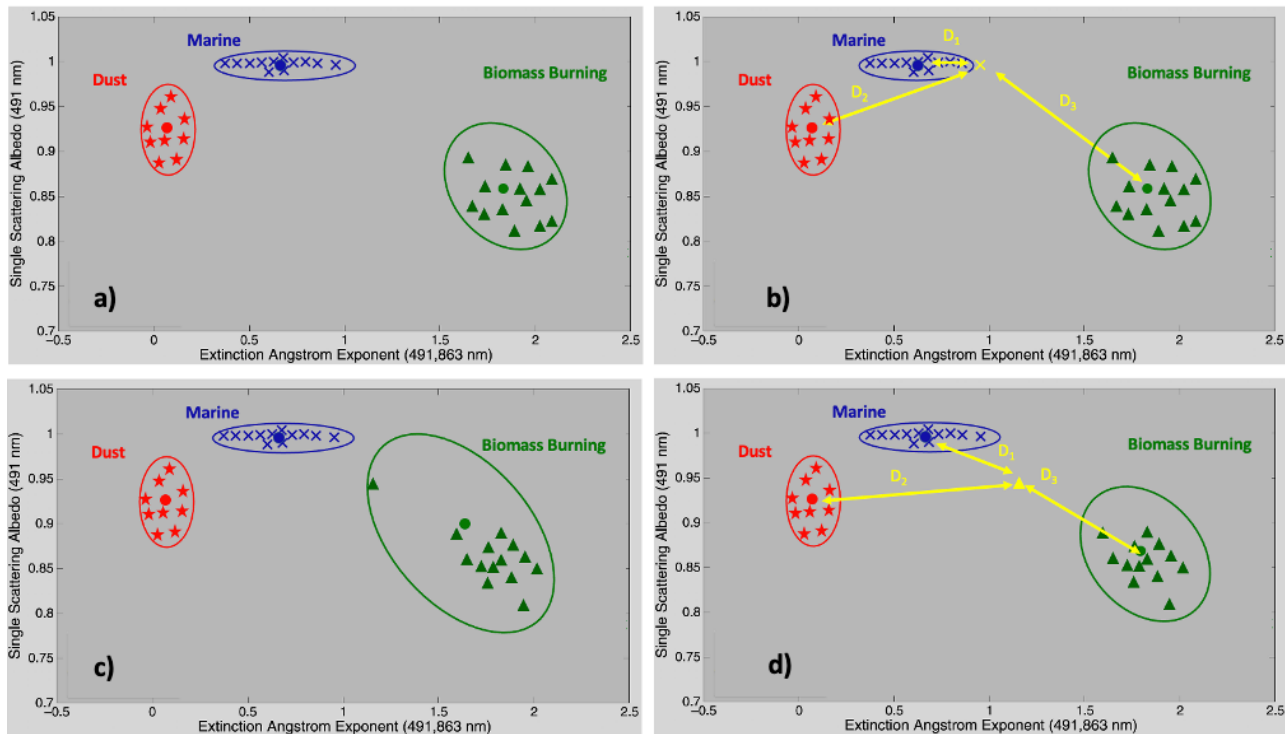
Name	Instrument	Aerosol Optical Parameters	Number of Points
AIRBO ₁	LARGE	EAE, SSA, dSSA, AC, AAE	871
AIRBO ₂	LARGE, DASH-SP	EAE, SSA, dSSA, AC, AAE, RRI	716
AIRBO ₃	LARGE, PI-Neph	EAE, SSA, dSSA, AC, AAE, RRI	176
AIRBO (This study)	LARGE, DASH-SP, PI-Neph	EAE, SSA, dSSA, AC, AAE, RRI	781

Table A1: Definition of three datasets (AIRBO₁, AIRBO₂, AIRBO₃) and their combination, AIRBO (which is the dataset used in this study), the airborne instruments involved during SEAC⁴RS (see Table 1), the co-located parameters (see Table 2 for a definition of EAE, SSA, dSSA, AC, AAE, and RRI) and the number of data points showing valid aerosol optical properties and PS-AMT BBAg., BBWild., Bio. or PollDust.

A.1.3 Method to Select Most Useful and Well Separated Aerosol Optical Properties

This section explains the second step of Fig. 1 in more details. Figure A1 is a simplified example to illustrate our method. It shows only two optical parameters (i.e., SSA and EAE) and three hypothetical PS-AMTs (e.g., “pure” dust in red, marine in blue and BB in green) measured by one hypothetical optical instrument in two different environments (defined by different locations and times, Fig. A1 a-b vs. A1 c-d). Fig A1 a-b shows a smaller hypothetical range of EAE and SSA for the BB PS-AMT (green cluster), compared to Fig. A1 c-d.

To answer the question “how well are these PS-AMTs (i.e., red, blue and green clusters in either Fig. A1 a or A1 c) separated?”, we (i) select each data point separately (e.g., yellow crosses on Fig A1 b and A1 d), (ii) recompute each PS-AMT cluster with the data point excluded (i.e., different blue PS-AMT on A1 b and green PS-AMT on A1 d compared to A1 a and A1 c) and calculate the Mahalanobis distance (Mahalanobis, 1936; Burton et al., 2012). The Mahalanobis distance is the distance between the data point in question (i.e., yellow crosses on Fig. A1 b or A1 d) and the position of each cluster center (i.e., red, blue, and green clusters on Fig. A1 b or A1 d), which depends on cluster center, tilt and width in a multi-parameter space. These distances are called D_1 , D_2 and D_3 on either Fig. A1 b or A1 d. In the case of the yellow cross on Fig. A1 b, distance D_1 is the smallest and the test point is reassigned to its original cluster. The test point is by consequence well separated from other clusters and “steady”. On the other hand, distance D_1 is also the smallest on Fig. A1 d, which means the test point (yellow cross) on Fig. A1 d is not reassigned to its original cluster. The test point is by consequence not well separated from other clusters in this case and not “steady”. The “steady fraction” is the fraction of cases within each PS-AMT that are correctly identified. “Steady” fractions are used to assess separation between PS-AMTs. When including additional components (e.g., any other aerosol optical parameter from Table 2 in addition to SSA and EAE on Fig. A1), the additional number of “steady points” shows the component’s relative importance in separating the PS-AMTs. The yellow points that are “steady” on Figure A1 (i.e., correctly classified, or well separated) are used to define the most useful and well separated aerosol optical properties for each PS-AMT.



900 **Figure A1: Conceptual/ hypothetical illustration of how we quantify separation between different**
air mass types, select the most useful and well separated aerosol optical parameters. It shows three
hypothetical PS-AMTs (e.g., dust in red, marine in blue and BB in green) measured by one
hypothetical optical instrument (Fig. A1 a-b) in one environment and another (Fig. A1 c-d). The
 905 **EAE and SSA values in this illustration are based on AERONET observations (Russell et al, 2014)**
and are representative of typical “pure” dust, marine and BB total column remote sensing inferred
ground based EAE and SSA values. Note that it only shows two dimensions even though some
calculations of Mahalanobis Distances (e.g., D_1 , D_2 , D_3) will be made using more dimensions in this
study.

910 **A.2 Additional Information on Results**

A.2.1 Aerosol Optical Parameters classified by PS-AMT

This section describes the ranges of the sixteen aerosol optical parameters (i.e., EAE, SSA, dSSA, AAE
 and AC at different combinations of 450, 550 and 700 nm and RRI at 532 nm from Table 2), classified
 by PS-AMTs in our study.

915

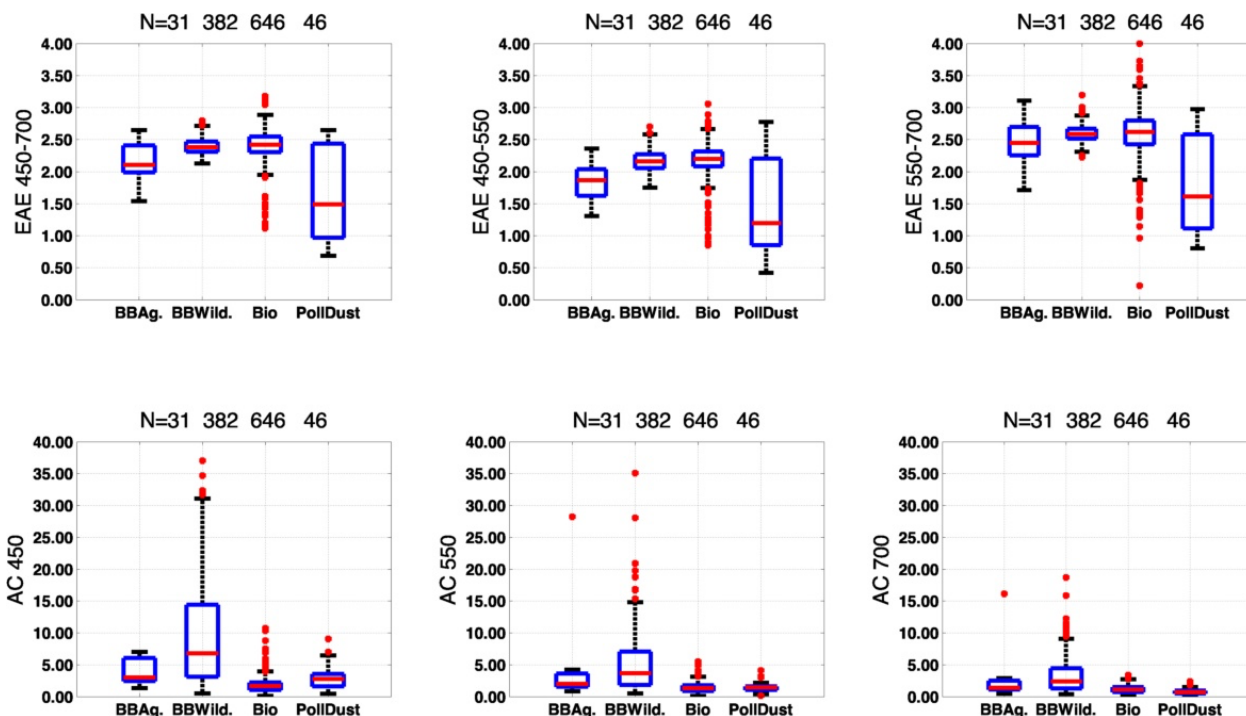


Figure A2: EAE (450-700nm, 450-550nm, 550-700nm) and AC (450, 550 and 700nm) per PS-AMTs. In each blue box, the red horizontal line indicates the median, and the bottom and top edges of the box indicate the 25th and 75th percentiles, respectively. The black whiskers extend to the most extreme data points not considered outliers, and the outliers are plotted individually using red points. Let us note that the LARGE EC measurements at 700 nm experienced issues during the latter half of SEAC⁴RS (Shinozuka et al., *pers. comm.*). AC: Absorption Coefficient, EAE: Extinction Angstrom Exponent. Numbers in the title correspond to the number of points behind each box-whisker for the respective BBAg, BBWild, Bio, and PollDust PS-AMTs.

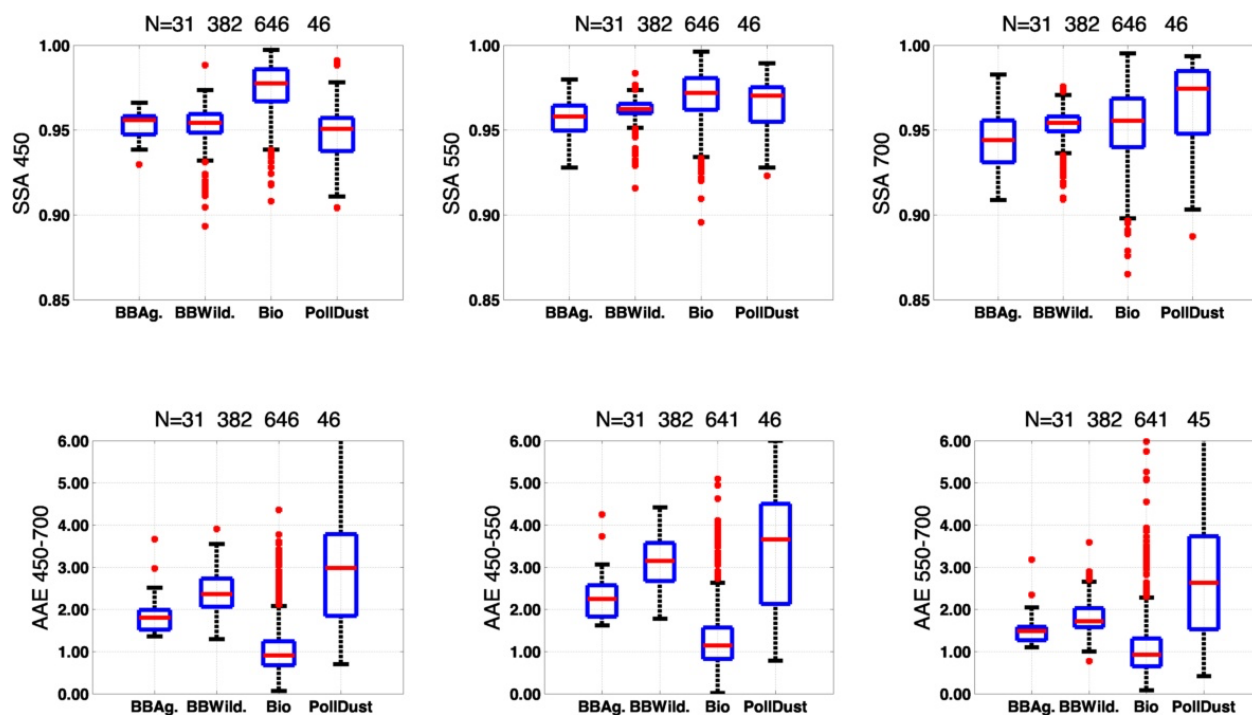


Figure A3: SSA (450, 550 and 700nm) and AAE (450-700nm, 450-550nm, 550-700nm) per PS-AMTs. In each blue box, the red horizontal line indicates the median, and the bottom and top edges of the box indicate the 25th and 75th percentiles, respectively. The black whiskers extend to the most extreme data points not considered outliers, and the outliers are plotted individually using red points. AAE: Absorption Angstrom Exponent, SSA: Single Scattering Albedo. Numbers in the title correspond to the number of points behind each box-whisker for the respective BBAg., BBWild., Bio. and PollDust PS-AMTs.

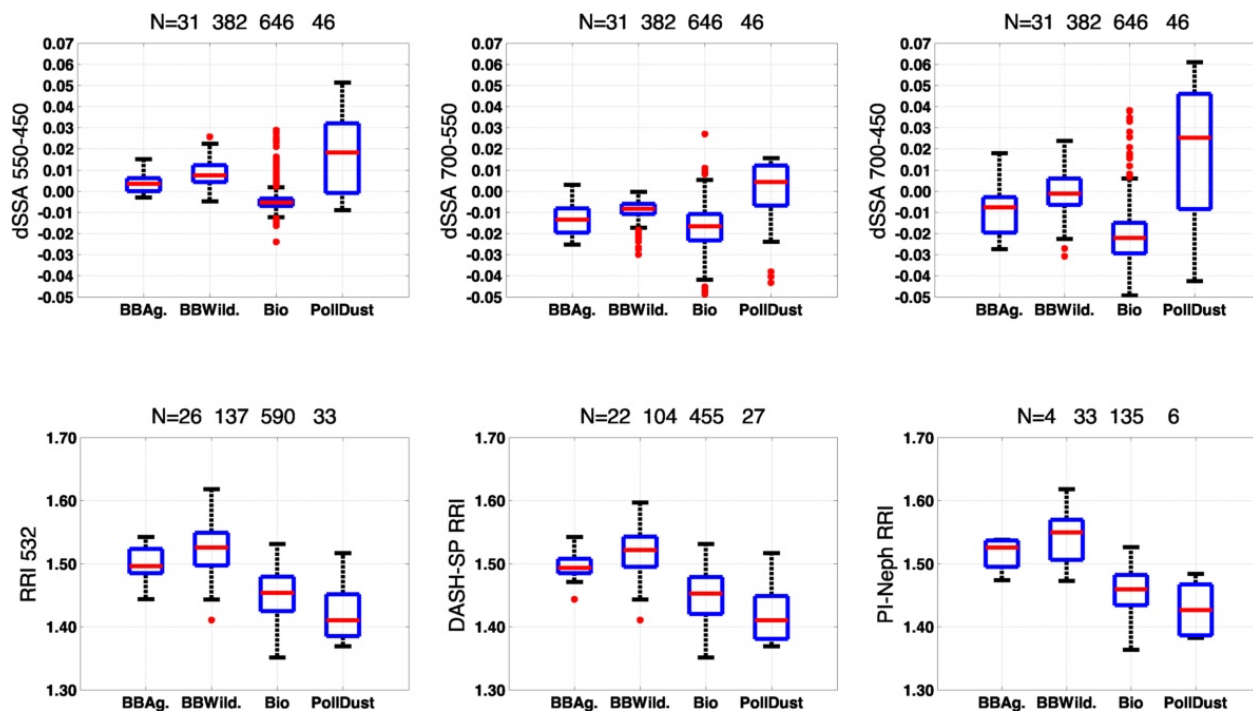
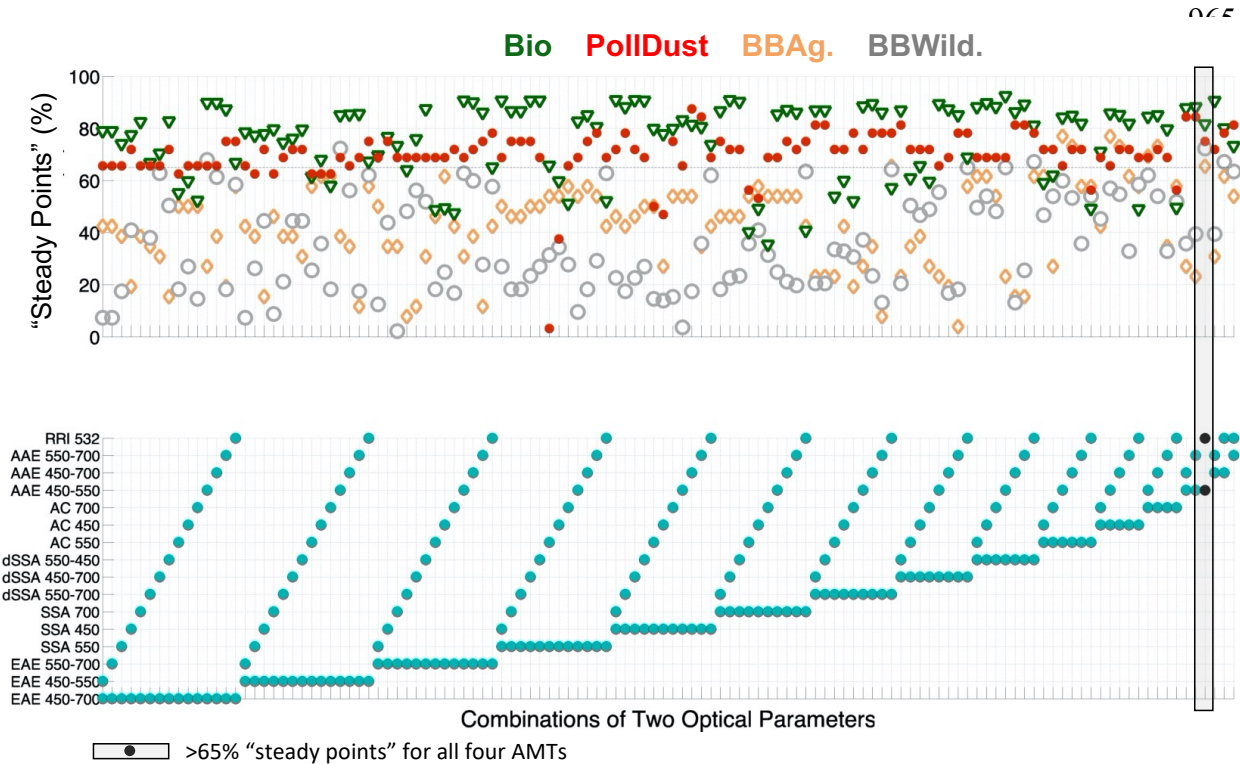


Figure A4: dSSA (700-450nm, 550-450nm, 700-550nm), RRI (from DASH-SP and PI-Neph), RRI from DASH-SP and RRI from PI-Neph at 532 nm per PS-AMTs. In each blue box, the red horizontal line indicates the median, and the bottom and top edges of the box indicate the 25th and 75th percentiles, respectively. The black whiskers extend to the most extreme data points not considered outliers, and the outliers are plotted individually using red points. RRI: Real Refractive Index, dSSA: difference in Single Scattering Albedo. Numbers in the title correspond to the number of points behind each box-whisker for the respective BBAg., BBWild., Bio. and PollDust PS-AMTs.

Note the slightly lower RRI values for DASH-SP, compared to PI-Neph (i.e., respectively 1.41 and 1.43 at 532nm in Fig. A4) in the case of PollDust PS-AMTs. We explain this difference in RRI values by different PollDust PS-AMT Growth Factor (GF) values. We obtain GF through two methods: (1) the values directly measured by DASH-SP for particles in the size range $0.18 < D_{p,dry} < 0.40 \mu\text{m}$ and (2) through an iterative procedure matching the output of a Mie code with dry PI-Neph retrievals and $f(\text{RH})$ measurements made by the LARGE group in parallel (see section A.1.1 for more details). We find a respective median PollDust PS-AMT GF value of ~ 1.3 and ~ 1.2 in the case of DASH-SP and PI-Neph, which we suggest is due to a smaller sampling size range for DASH-SP, compared to PI-Neph (see Table 1).

A.2.2 Most Useful and Well Separated Aerosol Optical Properties – Sixteen Parameters

960 This section describes the percentage of points unambiguously retrieved or “steady” (i.e., points that are well separated from other clusters and, hence, reassigned to their initial clusters) when using different combinations of respectively two and three out of sixteen aerosol optical parameters across all four principal PS-AMTs (i.e., provides more details to section 3.2).



990 **Figure A5: Percentage of “steady” points (i.e., fraction of cases of a given type that are correctly identified) in the upper panel when using different combinations of two aerosol optical parameters in the lower panel for each PS-AMT. The grey box and black points is a combination of optical parameters showing > 65% “steady” for PS-AMTs BBAg., BBWild., Bio.and PollDust. RRI: Real Refractive Index, AAE: Absorption Angstrom Exponent, AC: Absorption Coefficient, dSSA: difference in Single Scattering Albedo, SSA: Single Scattering Albedo, EAE: Extinction Angstrom Exponent.**

Fig.

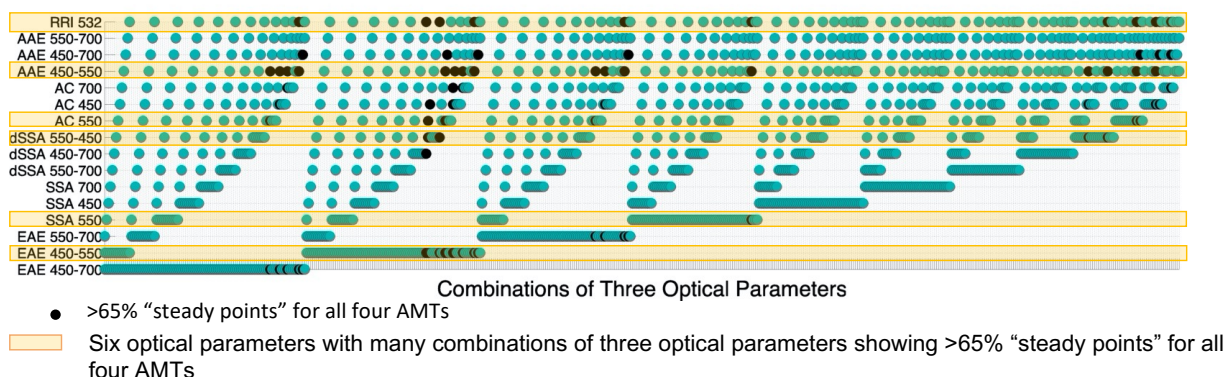
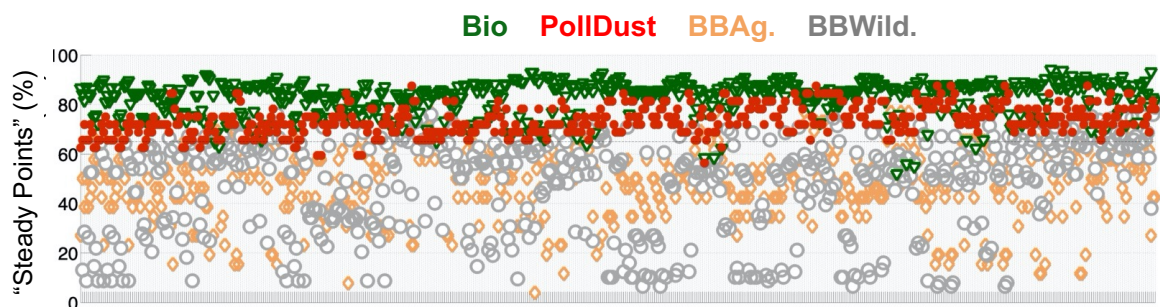


Figure A6: Percentage of "steady" points (i.e., fraction of cases of a given type that are correctly identified; see section 2.4 for more info) in the upper panel when using different combinations of three aerosol optical parameters in the lower panel for each PS-AMT. Black points are combinations of optical parameters showing > 65% "steady points" for PS-AMTs BBAg., BBWild., Bio. and PollDust. RRI: Real Refractive Index, AAE: Absorption Angstrom Exponent, AC: Absorption Coefficient, dSSA: difference in Single Scattering Albedo, SSA: Single Scattering Albedo, EAE: Extinction Angstrom Exponent. Horizontal orange boxes show the selection of our six aerosol optical parameters. Orange boxes show the six aerosol optical parameters that we have selected in this study.

A.2.3 Composition of our Polluted Dust (PollDust) PS-AMT

Fig. A7 shows a compositional picture of the PollDust PS-AMTs from PALMS. The accumulation mode is a mixture of particle types, all of which contain sulfate and organic material. Coarse mode dust particles account for most of the aerosol volume, whereas a non-dust accumulation mode contributes most to the total number concentration of particles.

015

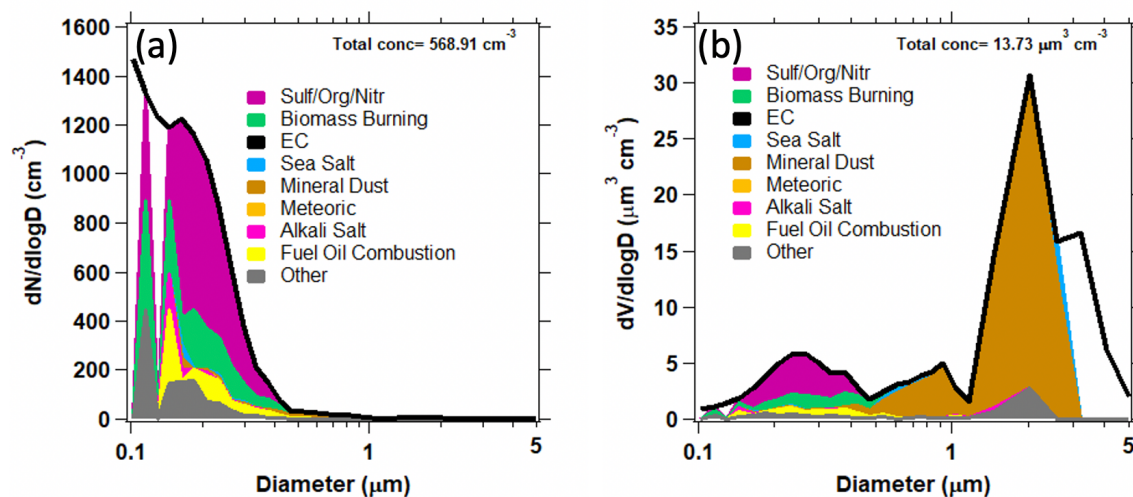


Figure A7: PALMS particle classes are mapped to the total number (a) and volume (b) size distribution from LARGE based on the method of Froyd et al. (2019). Data include flight segments representative of the Polluted Dust PS-AMT.

Appendix B

Abbreviations and acronyms

025	3MI	Multi-viewing Multi-channel Multi-polarization imager
	4STAR	Spectrometers for Sky-Scanning Sun-Tracking Atmospheric Research
	AAC	Absorption Angstrom Coefficient
	AAE	Absorption Angstrom Exponent
	AAOD	Aerosol Absorption Optical Depth
030	AC	Absorption Coefficient
	ACCP	Aerosol, Cloud, Convection and Precipitation
	AERONET	AERosol ROBotic NETwork
	AIMMS-20	Aircraft-Integrated Meteorological Measurement System
	Amm.	Ammonium
035	AMS	Aerosol Mass Spectroscopy
	AMT	Air Mass aerosol Types
	AOD	Aerosol Optical Depth
	APS	TSI Aerodynamic Particle Sizer
	BB	Biomass Burning Air Mass aerosol Types
040	BBAg.	Biomass Burning Agricultural Air Mass aerosol Types
	BBWild.	Biomass Burning Wildfire Air Mass aerosol Types
	BC	Black Carbon
	Bio.	Biogenic Air Mass aerosol Types
	Br.	Bromide
045	C ₂ O ₄	Oxalate
	Ca.	Calcium
	CALIOP	Cloud-Aerosol Lidar with Orthogonal Polarization
	CALIPSO	Cloud-Aerosol Lidar and Infrared Pathfinder Satellite Observation
	CAMP ² EX	Clouds, Aerosol and Monsoon Processes-Philippines Experiment
050	Cl	Chloride
	CO	Carbon monoxide
	CTM	Chemical Transport Models
	DACOM	Differential Absorption Carbon mOnoxide Monitor
	DASH-SP	Differential Aerosol Sizing and Hygroscopicity Spectrometer Probe
055	DO-Class	Defined Optical-based Classes
	DO-AMTs	Optical-based Air Mass aerosol Types
	Dp	particle diameter
	dNdl _{nr}	particle size distribution

	dSSA	difference in SSA at two wavelengths
060	dSSAC	difference in SSAC at two wavelengths
	EAC	Extinction Angstrom Coefficient
	EAE	Extinction Angstrom Exponent
	EC	Extinction Coefficient
	EOS	Earth Observing System
065	FIREX-AQ	Fire Influence on Regional to Global Environments and Air Quality
	GEOS-Chem	Goddard Earth Observing System- model of atmospheric CHEMistry
	GF	Growth Factor
	GRASP	Generalized Retrieval of Atmosphere and Surface Properties
	HARP2	Hyper-Angular Rainbow Polarimeter
070	HSKP	Housekeeping dataset
	K	potassium
	κ	particle hygroscopicity
	KORUS-AQ	An International Cooperative Air Quality Field Study in Korea
	LARGE	NASA Langley Aerosol Research group TSI nephelometer and Particle Soot Absorption
075	Photometer (PSAP) instruments	
	Mg	Magnesium
	MODIS	Moderate Resolution Imaging Spectroradiometer
	Na	Sodium
	Nit.	Nitrate
080	NO ₂	Nitrogen dioxide
	NO _y O ₃	NOAA Nitrogen Oxides and Ozone
	OA	Organic Aerosol
	PACE	NASA Plankton, Aerosol, Cloud, ocean Ecosystem
	PALMS	Particle Analysis by Laser Mass Spectrometry
085	PI-Neph	Polarized Imaging Nephelometer
	PM _{2.5}	Particulate Matter concentration with an aerodynamic diameter smaller than 2.5 μm
	POLDER	Polarization and Directionality of Earth's Reflectances
	PollDust	Polluted Dust Air Mass aerosol Types
	PS-AMTs	Prescribed Source-based Air Mass aerosol Types
090	PTR-MS	high-temperature Proton-Transfer-Reaction Mass Spectrometer
	RFari	Radiative Forcing due to aerosol-radiation interactions
	RH	Relative Humidity
	RI	complex Refractive Index
	RRI	Real part of the Refractive Index
095	SAGA	Soluble Acidic Gases and Aerosol
	SC	Scattering Coefficient
	SCMC	pre-Specified Clustering and Mahalanobis Classification method
	SEAC ⁴ RS	Study of Emissions and Atmospheric Composition, Clouds, and Climate Coupling by Regional Surveys
100	SEUS	Southeastern US

	SOA	Secondary Organic Aerosol
	SON	Sulfate-Organic-Nitrate
	SP2	NOAA Single Particle Soot Photometer
	SPEXone	Spectro-Polarimeter for Planetary Exploration orbital
105	SSA	Single Scattering Albedo
	SSAC	Single Scattering Albedo Coefficient
	Sul.	Sulfate
	T	Temperature
	TD-LIF	Thermal Dissociation and Laser Induced Fluorescence
110	US EPA	United States (of America) Environmental Protection Agency

Data Availability

The SEAC⁴RS data used in this study are publicly available at the following link: <https://www-air.larc.nasa.gov/cgi-bin/ArcView/seac4rs?DC8=#top>

Author Contribution

The overarching research goals were formulated by MSK. Many co-authors influenced the evolution of these research goals. MSK and QT carried out the formal analyses. MSK carried out the investigations and visualizations and wrote the original draft. All coauthors have reviewed and edited the multiple drafts of the paper. The methodology behind the SCMC method was first developed by SPB and adapted to *in situ* data by MSK.

Competing Interests

The authors declare that they have no conflict of interest, except for Dr Armin Sorooshian being an editor of ACP.

Acknowledgements

This research was supported by the NASA Atmospheric Composition Modeling and Analysis Program (ACMAP) under grant NNH14ZDA001N-ACMAP. We thank Dr R. Eckman for his support. PCJ and JLJ were supported by NASA 80NSSC21K1451 and 80NSSC19K0124. We appreciate the efforts of all the SEAC⁴RS *in situ* instrument principal investigators involved in this study for obtaining, processing, documenting, and disseminating their respective datasets. We also appreciate the comments of the reviewers that have helped us to improve this article.

References

- Adhikary, B., S. Kulkarni, A. Dallura, Y. Tang, T. Chai, L. R. Leung, Y. Qian, C. E. Chung, V. Ramanathan, and G. R. Carmichael: A regional scale chemical transport modeling of Asian aerosols with data assimilation of AOD observations using optimal interpolation technique, *Atmos. Environ.*, 42(37), 8600–8615, 2008.
- Aldhaif, A. M., Stahl, C., Braun, R. A., Moghaddam, M. A., Shingler, T., Crosbie, E., Sawamura, P., Dadashazar, H., Ziemba, L., Jimenez, J. L., Campuzano-Jost, P., and Sorooshian, A.: Characterization of the Real Part of Dry Aerosol Refractive Index Over North America From the Surface to 12 km, *J. Geophys. Res.-Atmos.*, 123, 8283–8300, <https://doi.org/10.1029/2018JD028504>, 2018.
- Benedetti, A., Morcrette, J.J., Boucher, O., Dethof, A., Engelen, R.J., Fisher, M., Flentje, H., Huneeus, N., Jones, L., Kaiser, J.W. and Kinne, S.: Aerosol analysis and forecast in the European Centre for Medium-Range Weather Forecasts Integrated Forecast System: 2. Data assimilation, *J. Geophys. Res.-Atmos.*, 114 (D13), <https://doi.org/10.1029/2008JD011115>, 2009.
- National Academies of Sciences, Engineering, and Medicine: Thriving on Our Changing Planet: A Decadal Strategy for Earth Observation from Space, The National Academies Press, Washington, D.C., 2018.
- Bohren, C. F. and Huffman, D. R.: *Absorption and Scattering of Light by Small Particles*, John Wiley & Sons, 1983.
- Bond, T.C., Doherty, S.J., Fahey, D.W., Forster, P.M., Berntsen, T., DeAngelo, B.J., Flanner, M.G., Ghan, S., Kärcher, B., Koch, D. and Kinne, S.: Bounding the role of black carbon in the climate system: A scientific assessment, *J. Geophys. Res.-Atmos.*, 118(11), <https://doi.org/10.1002/jgrd.50171>, 5380–5552, 2013.
- Boucher, O., Randall, D., Artaxo, P., Bretherton, C., Feingold, G., Forster, P., Kerminen, V.-M., Kondo, Y., Liao, H., Lohmann, U., Rasch, P., Satheesh, S. K., Sherwood, S., Stevens, B., and Zhang, X. Y.: Clouds and aerosols, in: *Climate Change 2013: The Physical Science Basis. Contribution of Working Group I to the Fifth Assessment Report of the Intergovernmental Panel on Climate Change*, edited by: Stocker, T. F., Qin, D., Plattner, G.-K., Tignor, M., Allen, S. K., Doschung, J., Nauels, A., Xia, Y., Bex, V., and Midgley, P. M.: Cambridge University Press, United Kingdom and New York USA, 571–657, doi:10.1017/CBO9781107415324.016, 2013.
- Buchard, V., Randles, C.A., Da Silva, A.M., Darmenov, A., Colarco, P.R., Govindaraju, R., Ferrare, R., Hair, J., Beyersdorf, A.J., Ziemba, L.D. and Yu, H.: The MERRA-2 aerosol reanalysis, 1980 onward. Part II: Evaluation and case studies, *J. Climate*, 30(17), 6851–6872, 2017.

- Burton, S. P., Ferrare, R. A., Hostetler, C. A., Hair, J. W., Rogers, R. R., Obland, M. D., Butler, C. F., Cook, A. L., Harper, D. B., and Froyd, K. D.: Aerosol classification using airborne High Spectral Resolution Lidar measurements – methodology and examples, *Atmos. Meas. Tech.*, 5, 73–98, <https://doi.org/10.5194/amt-5-73-2012>, 2012.
- Canagaratna, M. R., Jayne, J. T., Jimenez, J. L., Allan, J. D., Alfarra, M. R., Zhang, Q., Onasch, T. B., Drewnick, F., Coe, H., Middlebrook, A., Delia, A., Williams, L. R., Trimborn, A. M., Northway, M. J., DeCarlo, P. F., Kolb, C. E., Davidovits, P., and Worsnop, D. R.: Chemical and microphysical characterization of ambient aerosols with the aerodyne aerosol mass spectrometer, *Mass Spectrom. Rev.*, 26(2), 185–222, <https://doi.org/10.1002/mas.20115>, 2007.
- Chen, C., Dubovik, O., Henze, D. K., Lapyonak, T., Chin, M., Ducos, F., Litvinov, P., Huang, X., and Li, L.: Retrieval of desert dust and carbonaceous aerosol emissions over Africa from POLDER/PARASOL products generated by the GRASP algorithm, *Atmos. Chem. Phys.*, 18, 12551–12580, <https://doi.org/10.5194/acp-18-12551-2018>, 2018.
- Chen, C., Dubovik, O., Henze, D. K., Chin, M., Lapyonok, T., Schuster, G. L., Ducos, F., Fuertes, D., Litvinov, P., Li, L., Lopatin, A., Hu, Q., and Torres, B.: Constraining global aerosol emissions using POLDER/PARASOL satellite remote sensing observations, *Atmos. Chem. Phys.*, 19, 14585–14606, <https://doi.org/10.5194/acp-19-14585-2019>, 2019.
- Chin, M., Ginoux, P., Kinne, S., Torres, O., Holben, B., Duncan, B., Martin, R., Logan, J., Higurashi, A., and Nakajima, T.: Tropospheric aerosol optical thickness from the GOCART model and comparisons with satellite and sunphotometer measurements, *J. Atmos. Sci.*, 59(3), 461–483, 2002.
- Cleary, P. A., Wooldridge, P. J., and Cohen, R. C.: Laser-induced fluorescence detection of atmospheric NO₂ using a commercial diode laser and a supersonic expansion, *Appl. Opt.*, 41, 6950–6956, 2002.
- Collins, W.D., Rasch, P.J., Eaton, B.E., Khattatov, B.V., Lamarque, J.F. and Zender, C.S.: Simulating aerosols using a chemical transport model with assimilation of satellite aerosol retrievals: Methodology for INDOEX, *J. Geophys. Res.-Atmos.*, 106(D7), 7313–7336, <https://doi.org/10.1029/2000JD900507>, 2001.
- Cubison, M. J., Ortega, a. M., Hayes, P. L., Farmer, D. K., Day, D., Lechner, M. J., Brune, W. H., Apel, E., Diskin, G. S., Fisher, J. a., Fuelberg, H. E., Hecobian, A., Knapp, D. J., Mikoviny, T., Riemer, D., Sachse, G. W., Sessions, W., Weber, R. J., Weinheimer, a. J., Wisthaler, A., and Jimenez, J. L.: Effects of aging on organic aerosol from open biomass burning smoke in aircraft and laboratory studies, *Atmos. Chem. Phys.*, 11, 12049–12064, <https://doi.org/10.5194/acp-11-12049-2011>, 2011.
- Daellenbach, K. R., Uzu, G., Jiang, J., Cassagnes, L.-E., Leni, Z., Vlachou, A., Stefenelli, G., Canonaco, F., Weber, S., Segers, A., Kuenen, J. J. P., Schaap, M., Favez, O., Albinet, A., Aksoyoglu, S., Dommen, J., Baltensperger, U., Geiser, M., El Haddad, I., Jaffrezo, J.-L., and Prévôt, A. S. H.: Sources of

- particulate-matter air pollution and its oxidative potential in Europe, *Nature*, 587, 414–419,
215 <https://doi.org/10.1038/s41586-020-2902-8>, 2020.
- Dawson, K.W., Meskhidze, N., Burton, S.P., Johnson, M.S., Kacenelenbogen, M.S., Hostetler, C.A. and
Hu, Y.: Creating Aerosol Types from Chemistry (CATCH): A new algorithm to extend the link between
remote sensing and models, *J. Geophys. Res.-Atmos.*, 122(22), 12-366,
220 <https://doi.org/10.1002/2017JD026913>, 2017.
- DeCarlo, P. F., Kimmel, J. R., Trimborn, A., Northway, M. J., Jayne, J. T., Aiken, A. C., Gonin, M.,
Fuhrer, K., Horvath, T., Docherty, K. S., Worsnop, D. R., and Jimenez, J. L.: Field-deployable, high-
resolution, time-of-flight aerosol mass spectrometer, *Anal. Chem.*, 78, 8281–8289, 2006.
- 225 Deuzé, J.-L., Bréon, F.-M., Devaux, C., Goloub, P., Herman, M., Lafrance, B., Maignan, F., Marchand,
A., Nadal, F., Perry, G., and Tanré, D.: Remote sensing of aerosols over land surfaces from POLDER-
ADEOS-1 polarized measurements, *J. Geophys. Res.-Atmos.*, 106(D5), 4913–4926,
<https://doi.org/10.1029/2000JD900364>, 2001.
- 230 Dobb, Jack E., Robert W. Talbot, Eric M. Scheuer, Garry Seid, Melody A. Avery, and Hanwant B. Singh:
Aerosol chemical composition in Asian continental outflow during the TRACE-P campaign: Comparison
with PEM-West B, *J. Geophys. Res.-Atmos.*, 108 (D21), <https://doi.org/10.1029/2002JD003111>, 2003.
- 235 Dolgos, G. and Martins, J. V.: Polarized Imaging Nephelometer for in situ airborne measurements of
aerosol light scattering, *Opt. Express*, 22, 21972–21990, 2014.
- Dubovik, O., Lapyonok, T., Litvinov, P., Herman, M., Fuertes, D., Ducos, F., Lopatin, A., Chaikovsky,
A., Torres, B., Derimian, Y., Xin Huang, Aspetsberger, M., and Federspiel, C.: GRASP: a versatile
240 algorithm for characterizing the atmosphere, *SPIE Newsroom*, doi:10.1117/2.1201408.005558, 2014.
- Dunagan, S. E., Johnson, R., Zavaleta, J., Russell, P. B., Schmid, B., Flynn, C., Redemann, J., Shinozuka,
Y., Livingston, J., and Segal-Rosenhaimer, M.: Spectrometer for Sky-Scanning Sun-Tracking
Atmospheric Research (4STAR): Instrument Technology, *Remote Sensing*, 5, 3872–3895,
245 <https://doi.org/10.3390/rs5083872>, 2013.
- Eck, T.F., Holben, B.N., Reid, J.S., Mukelabai, M.M., Piketh, S.J., Torres, O., Jethva, H.T., Hyer, E.J.,
Ward, D.E., Dubovik, O. and Sinyuk, A.: A seasonal trend of single scattering albedo in southern African
biomass-burning particles: Implications for satellite products and estimates of emissions for the world's
250 largest biomass-burning source, *J. Geophys. Res.-Atmos.*, 118(12), 6414-6432,
<https://doi.org/10.1002/jgrd.50500>, 2013.
- Edgerton, E. S., Hartsell, B. E., Saylor, R. D., Jansen, J. J., Hansen, D. A., and Hidy, G. M.: The
Southeastern Aerosol Research and Characterization Study, Part 3: Continuous measurements of fine
255 particulate matter mass and composition, *J. Air Waste Manage.*, 56, 1325–1341, 2006.

- 260 Espinosa, W. R., Remer, L. A., Dubovik, O., Ziemba, L., Beyersdorf, A., Orozco, D., Schuster, G., Lapyonok, T., Fuertes, D., and Martins, J. V.: Retrievals of aerosol optical and microphysical properties from Imaging Polar Nephelometer scattering measurements, *Atmos. Meas. Tech.*, 10, 811–824, <https://doi.org/10.5194/amt-10-811-2017>, 2017.
- 265 Espinosa, W. R., Martins, J. V., Remer, L. A., Puthukkudy, A., Orozco, D., & Dolgos, G: *In situ* measurements of angular-dependent light scattering by aerosols over the contiguous United States. *Atmos. Chem. Phys.*, 18, 3737–3754, <https://doi.org/10.5194/acp-18-3737-2018>, 2018.
- 270 Forrister, H., Liu, J., Scheuer, E., Dibb, J., Ziemba, L., Thornhill, K. L., Anderson, B., Diskin, G., Perring, A. E., Schwarz, J. P., Campuzano-Jost, P., Day, D. A., Palm, B. B., Jimenez, J. L., Nenes, A., and Weber, R. J.: Evolution of brown carbon in wildfire plumes, *Geophys. Res. Lett.*, 42, 4623–4630, <https://doi.org/10.1002/2015gl063897>, 2015.
- 275 Fougnie, B., Marbach, T., Lacan, A., Lang, R., Schlüssel, P., Poli, G., Munro, R., and Couto, A. B.: The multi-viewing multi-channel multi-polarisation imager – Overview of the 3MI polarimetric mission for aerosol and cloud characterization, *J. Quant. Spectrosc. Ra.*, 219, 23–32, <https://doi.org/10.1016/j.jqsrt.2018.07.008>, 2018.
- Fried, A., Diskin, G., Weibring, P., Richter, D., Walega, J. G., Sachse, G., Slate, T., Rana, M., and Podolske, J.: Tunable infrared laser instruments for airborne atmospheric studies, *Appl. Phys. B*, 92(3), 409–417, 2008.
- 280 Froyd, K. D., Murphy, D. M., Brock, C. A., Campuzano-Jost, P., Dibb, J. E., Jimenez, J.-L., Kupc, A., Middlebrook, A. M., Schill, G. P., Thornhill, K. L., Williamson, C. J., Wilson, J. C., and Ziemba, L. D.: A new method to quantify mineral dust and other aerosol species from aircraft platforms using single-particle mass spectrometry, *Atmos. Meas. Tech.*, 12, 6209–6239, <https://doi.org/10.5194/amt-12-6209-2019>, 2019.
- 285 Fu, G., Hasekamp, O., Rietjens, J., Smit, M., Di Noia, A., Cairns, B., Wasilewski, A., Diner, D., Seidel, F., Xu, F., Knobelspiesse, K., Gao, M., da Silva, A., Burton, S., Hostetler, C., Hair, J., and Ferrare, R.: Aerosol retrievals from different polarimeters during the ACEPOL campaign using a common retrieval algorithm, *Atmos. Meas. Tech.*, 13, 553–573, <https://doi.org/10.5194/amt-13-553-2020>, 2020.
- 290 Generoso, S., F.-M. Bréon, F. Chevallier, Y. Balkanski, M. Schulz, and I. Bey, Assimilation of POLDER aerosol optical thickness into the LMDz-INCA model: Implications for the Arctic aerosol burden, *J. Geophys. Res.-Atmos.*, 112(D2), <https://doi.org/10.1029/2005JD006954>, 2007.
- 295 Guo H., Pedro Campuzano-Jost, Demetrios Pagonis, Melinda Schueneman, Doug A Day, Benjamin A Nault, Dongwook Kim, Wyatt Brown, Kyla S.A. Siemens, Jack E Dibb, Eric M Scheuer, Laura Tomsche, Felix Piel, John B Nowak, Armin Wisthaler, Lu Xu, Krystal Vasquez, John D Crounse, Paul O Wennberg,

- Pamela Rickly, Andrew W Rollins, Caroline Womack, Joseph M Katich, Anne Elizabeth Perring, Hannah S Halliday, Amber Jeanine Soja, Emily Marie Gargulinski, Elizabeth Brooke Wiggins, Jessica L McCarty, Glenn S Diskin, Thomas F Hanisco, Alexander Laskin and Jose L Jimenez, Submicron Particle Composition and Acidity in Fire Plumes during FIREX-AQ aircraft study, American Geosciences Union fall meeting, A232-10, December 2020.
- Guo, H., Campuzano-Jost, P., Nault, B. A., Day, D. A., Schroder, J. C., Kim, D., Dibb, J. E., Dollner, M., Weinzierl, B., and Jimenez, J. L.: The importance of size ranges in aerosol instrument intercomparisons: a case study for the Atmospheric Tomography Mission, *Atmos. Meas. Tech.*, 14, 3631–3655, <https://doi.org/10.5194/amt-14-3631-2021>, 2021.
- Hänel, G.: The properties of atmospheric aerosol particles as functions of the relative humidity at thermodynamic equilibrium with the surrounding moist air, *Adv. Geophys.*, 19, 73–188, 1976.
- Hasekamp, O. P., P. Litvinov, and A. Butz, Aerosol properties over the ocean from PARASOL multiangle photopolarimetric measurements, *J. Geophys. Res.-Atmos.*, 116(D14), <https://doi.org/10.1029/2010JD015469>, 2011.
- Hasekamp, O. P., Fu, G., Rusli, S. P., Wu, L., Di Noia, A., aan de Brugh, J., Landgraf, J., Smit, J. M., Rietjens, J., and van Amerongen, A.: Aerosol Measurements by SPEXone on the NASA PACE Mission: expected retrieval capabilities, *J. Quant. Spectrosc. Ra.*, 224, 474-511, 2019.
- Hecobian, A., Liu, Z., Hennigan, C. J., Huey, L. G., Jimenez, J. L., Cubison, M. J., Vay, S., Diskin, G. S., Sachse, G. W., Wisthaler, A., Mikoviny, T., Weinheimer, a. J., Liao, J., Knapp, D. J., Wennberg, P. O., Kürten, A., Crounse, J. D., Clair, J. S., Wang, Y., and Weber, R. J.: Comparison of chemical characteristics of 495 biomass burning plumes intercepted by the NASA DC-8 aircraft during the ARCTAS/CARB-2008 field campaign, *Atmos. Chem. Phys.*, 11, 13325–13337, <https://doi.org/10.5194/acp-11-13325-2011>, 2011.
- Herman, M., Deuzé, J.L., Marchand, A., Roger, B. and Lallart, P.: Aerosol remote sensing from POLDER/ADEOS over the ocean: Improved retrieval using a nonspherical particle model, *J. Geophys. Res.-Atmos.*, 110(D10), <https://doi.org/10.1029/2004JD004798>, 2005.
- Hodzic, A., Campuzano-Jost, P., Bian, H., Chin, M., Colarco, P. R., Day, D. A., Froyd, K. D., Heinold, B., Jo, D. S., Katich, J. M., Kodros, J. K., Nault, B. A., Pierce, J. R., Ray, E., Schacht, J., Schill, G. P., Schroder, J. C., Schwarz, J. P., Sueper, D. T., Tegen, I., Tilmes, S., Tsigaridis, K., Yu, P., and Jimenez, J. L.: Characterization of organic aerosol across the global remote troposphere: a comparison of ATom measurements and global chemistry models, *Atmos. Chem. Phys.*, 20, 4607–4635, <https://doi.org/10.5194/acp-20-4607-2020>, 2020.
- Holben, B. N., Eck, T. F., Slutsker, I., Tanre, D., Buis, J. P., Setzer, A., Vermote, E., Reagan, J. A., Kaufman, Y. J., Nakajima, T., Lavenu, F., Jankowiak, I., and Smirnov, A.: AERONET – A federated

- instrument network and data archive for aerosol characterization, *Remote Sens. Environ.*, 66, 1–16, doi:10.1016/S00344257(98)00031-5, 1998.
- Hu, W. W., Campuzano-Jost, P., Palm, B. B., Day, D. A., Ortega, A. M., Hayes, P. L., Krechmer, J. E., Chen, Q., Kuwata, M., Liu, Y. J., de Sá, S. S., McKinney, K., Martin, S. T., Hu, M., Budisulistiorini, S. H., Riva, M., Surratt, J. D., St. Clair, J. M., Isaacman-Van Wertz, G., Yee, L. D., Goldstein, A. H., Carbone, S., Brito, J., Artaxo, P., de Gouw, J. A., Koss, A., Wisthaler, A., Mikoviny, T., Karl, T., Kaser, L., Jud, W., Hansel, A., Docherty, K. S., Alexander, M. L., Robinson, N. H., Coe, H., Allan, J. D., Canagaratna, M. R., Paulot, F., and Jimenez, J. L.: Characterization of a real-time tracer for isoprene epoxydiols-derived secondary organic aerosol (IEPOX-SOA) from aerosol mass spectrometer measurements, *Atmos. Chem. Phys.*, 15, 11807–11833, <https://doi.org/10.5194/acp-15-11807-2015>, 2015.
- Jo, D. S., Hodzic, A., Emmons, L. K., Marais, E. A., Peng, Z., Nault, B. A., Hu, W., Campuzano-Jost, P., and Jimenez, J. L.: A simplified parameterization of isoprene-epoxydiol-derived secondary organic aerosol (IEPOX-SOA) for global chemistry and climate models: a case study with GEOS-Chem v11-02-rc, *Geosci. Model Dev.*, 12, 2983–3000, <https://doi.org/10.5194/gmd-12-2983-2019>, 2019.
- Johnson, M. S., Meskhidze, N., and Kiliyanpilakkil, V. P.: A global comparison of GEOS-Chem-predicted and remotely-sensed mineral dust aerosol optical depth and extinction profiles, *J. Adv. Model. Earth Syst.*, 4, M07001, doi:10.1029/2011MS000109, 2012.
- Jolleys, M. D., Coe, H., McFiggans, G., Taylor, J. W., O'Shea, S. J., Le Breton, M., Bauguitté, S. J.-B., Moller, S., Di Carlo, P., Aruffo, E., Palmer, P. I., Lee, J. D., Percival, C. J., and Gallagher, M. W.: Properties and evolution of biomass burning organic aerosol from Canadian boreal forest fires, *Atmos. Chem. Phys.*, 15, 3077–3095, <https://doi.org/10.5194/acp-15-3077-2015>, 2015.
- Kahnert, M.: Variational data analysis of aerosol species in a regional CTM: background error covariance constraint and aerosol optical observation operators, *Tellus B*, 60, 753–770, doi:10.1111/j.1600-0889.2008.00377.x, 2008.
- Kim, P. S., Jacob, D. J., Fisher, J. A., Travis, K., Yu, K., Zhu, L., Yantosca, R. M., Sulprizio, M. P., Jimenez, J. L., Campuzano-Jost, P., Froyd, K. D., Liao, J., Hair, J. W., Fenn, M. A., Butler, C. F., Wagner, N. L., Gordon, T. D., Welti, A., Wennberg, P. O., Crounse, J. D., St. Clair, J. M., Teng, A. P., Millet, D. B., Schwarz, J. P., Markovic, M. Z., and Perring, A. E.: Sources, seasonality, and trends of southeast US aerosol: an integrated analysis of surface, aircraft, and satellite observations with the GEOS-Chem chemical transport model, *Atmos. Chem. Phys.*, 15, 10411–10433, <https://doi.org/10.5194/acp-15-10411-2015>, 2015.
- Kondo, Y., Sahu, L., Moteki, N., Khan, F., Takegawa, N., Liu, X., Koike, M., and Miyakawa, T.: Consistency and traceability of black carbon measurements made by laser-induced incandescence,

- thermal-optical transmittance, and filter-based photoabsorption techniques, *Aerosol Sci. Technol.*, 45, 295–312, doi:10.1080/02786826.2010.533215, 2011.
- 385 Kumar, R., Delle Monache, L., Bresch, J., Saide, P.E., Tang, Y., Liu, Z., da Silva, A.M., Alessandrini, S., Pfister, G., Edwards, D. and Lee, P.: Toward improving short-term predictions of fine particulate matter over the United States via assimilation of satellite aerosol optical depth retrievals, *J. Geophys. Res.-Atmos.*, 124(5), 2753–2773, <https://doi.org/10.1029/2018JD029009>, 2019.
- 390 Landrigan, P. J., Fuller, R., Acosta, N. J. R., Adeyi, O., Arnold, R., Basu, N. (nil), Baldé, A. B., Bertollini, R., Bose-O'Reilly, S., Boufford, J. I., Breyse, P. N., Chiles, T., Mahidol, C., Coll-Seck, A. M., Cropper, M. L., Fobil, J., Fuster, V., Greenstone, M., Haines, A., Hanrahan, D., Hunter, D., Khare, M., Krupnick, A., Lanphear, B., Lohani, B., Martin, K., Mathiasen, K. V., McTeer, M. A., Murray, C. J. L., Ndahimananjara, J. D., Perera, F., Potočník, J., Preker, A. S., Ramesh, J., Rockström, J., Salinas, C., Samson, L. D., Sandilya, K., Sly, P. D., Smith, K. R., Steiner, A., Stewart, R. B., Suk, W. A., van Schayck, 395 O. C. P., Yadama, G. N., Yumkella, K., and Zhong, M.: The Lancet Commission on pollution and health, *The Lancet*, 391(10119), 462–512, 2018.
- Lanzi, E.: *The Economic Consequences of Outdoor Air Pollution*. Organization for Economic Cooperation and Development (OECD) Publishing, Paris, <http://dx.doi.org/10.1787/9789264257474-en>, 400 Retrieved from <https://www.oecd.org/environment/indicators-modelling-outlooks/Policy-Highlights-Economic-consequences-of-outdoor-air-pollution-web.pdf>, 2016.
- Laskin, A., Laskin, J., and Nizkorodov, S. A.: Chemistry of Atmospheric Brown Carbon, *Chem. Rev.*, 115, 4335–4382, 2015. 405
- Lelieveld, J., Evans, J.S., Fnais, M., Giannadaki, D. and Pozzer, A., The contribution of outdoor air pollution sources to premature mortality on a global scale, *Nature*, 525(7569), 367–371, <https://doi.org/10.1038/nature15371>, 2015.
- 410 Lelieveld, J., Klingmüller, K., Pozzer, A., Pöschl, U., Fnais, M., Daiber, A., and Münzel, T.: Cardiovascular disease burden from ambient air pollution in Europe reassessed using novel hazard ratio functions, *Eur. Heart J.*, 40, 1590–1596, <https://doi.org/10.1093/eurheartj/ehz135>, 2019
- Liao, J., Froyd, K. D., Murphy, D. M., Keutsch, F. N., Yu, G., Wennberg, P. O., St. Clair, J. M., Crounse, 415 J. D., Wisthaler, A., Mikoviny, T., Jimenez, J. L., Campuzano-Jost, P., Day, D. A., Hu, W., Ryerson, T. B., Pollack, I. B., Peischl, J., Anderson, B. E., Ziemba, L. D., Blake, D. R., Meinardi, S., and Diskin, G.: Airborne measurements of organosulfates over the continental U. S., *J. Geophys. Res.-Atmos.*, 120(7), 2990–3005, <https://doi.org/10.1002/2014JD022378>, 2015.
- 420 Lim, S. S., Vos, T., Flaxman, A. D., Danaei, G., Shibuya, K., AdairRohani, H., AlMazroa, M. A., Amann, M., Anderson, H. R., Andrews, K. G., Aryee, M., Atkinson, C., Bacchus, L. J., Bahalim, A. N., Balakrishnan, K., Balmes, J., Barker-Collo, S., Baxter, A., Bell, M. L., Blore, J. D., Blyth, F., Bonner, C.,

- Borges, G., Bourne, R., Boussinesq, M., Brauer, M., Brooks, P., Bruce, N. G., Brunekreef, B., Bryan-Hancock, C., Bucello, C., Buchbinder, R., Bull, F., Burnett, R. T., Byers, T. E., Calabria, B., Carapetis, J., Carnahan, E., Chafe, Z., Charlson, F., Chen, H., Chen, J. S., Cheng, A. T.-A., Child, J. C., Cohen, A., Colson, K. E., Cowie, B. C., Darby, S., Darling, S., Davis, A., Degenhardt, L., Dentener, F., Des Jarlais, D. C., Devries, K., Dherani, M., Ding, E. L., Dorsey, E. R., Driscoll, T., Edmond, K., Ali, S. E., Engell, R. E., Erwin, P. J., Fahimi, S., Falder, G., Farzadfar, F., Ferrari, A., Finucane, M. M., Flaxman, S., Fowkes, F. G. R., Freedman, G., Freeman, M. K., Gakidou, E., Ghosh, S., Giovannucci, E., Gmel, G., Graham, K., Grainger, R., Grant, B., Gunnell, D., Gutierrez, H. R., Hall, W., Hoek, H. W., Hogan, A., Hosgood, H. D., Hoy, D., Hu, H., Hubbell, B. J., Hutchings, S. J., Ibeanusi, S. E., Jacklyn, G. L., Jasrasaria, R., Jonas, J. B., Kan, H., Kanis, J. A., Kassebaum, N., Kawakami, N., Khang, Y.-H., Khatibzadeh, S., Khoo, J.-P., et al.: A comparative risk assessment of burden of disease and injury attributable to 67 risk factors and risk factor clusters in 21 regions, 1990–2010: a systematic analysis for the Global Burden of Disease Study 2010, *The Lancet*, 380, 2224–2260, [https://doi.org/10.1016/S0140-6736\(12\)61766-8](https://doi.org/10.1016/S0140-6736(12)61766-8), 2012.
- Lin, C., Wang, Z., and Zhu, J.: An Ensemble Kalman Filter for severe dust storm data assimilation over China, *Atmos. Chem. Phys.*, 8, 2975–2983, <https://doi.org/10.5194/acp-8-2975-2008>, 2008.
- Liu, X., Zhang, Y., Huey, L.G., Yokelson, R.J., Wang, Y., Jimenez, J.L., Campuzano-Jost, P., Beyersdorf, A.J., Blake, D.R., Choi, Y. and St. Clair, J.M.: Agricultural fires in the southeastern U.S. during SEAC4RS: Emissions of trace gases and particles and evolution of ozone, reactive nitrogen, and organic aerosol, *J. Geophys. Res.-Atmos.*, 121(12), 7383–7414, <https://doi.org/10.1002/2016JD025040>, 2016.
- Liu, X., Huey, L.G., Yokelson, R.J., Selimovic, V., Simpson, I.J., Müller, M., Jimenez, J.L., Campuzano-Jost, P., Beyersdorf, A.J., Blake, D.R. and Butterfield, Z.: Airborne measurements of western U.S. wildfire emissions: Comparison with prescribed burning and air quality implications, *J. Geophys. Res.-Atmos.*, 122, 6108–6129, <https://doi.org/10.1002/2016JD026315>, 2017.
- Loeb, Norman G., and Wenying Su.: Direct aerosol radiative forcing uncertainty based on a radiative perturbation analysis, *J. Climate*, 23(19), 5288–5293, <https://doi.org/10.1175/2010JCLI3543.1>, 2010.
- Ma, C., Wang, T., Mizzi, A.P., Anderson, J.L., Zhuang, B., Xie, M. and Wu, R.: Multiconstituent data assimilation with WRF-Chem/DART: Potential for adjusting anthropogenic emissions and improving air quality forecasts over eastern China, *J. Geophys. Res.-Atmos.*, 124(13), 7393–7412, <https://doi.org/10.1029/2019JD030421>, 2019.
- Mahalanobis, P. C.: On the generalized distance in statistics, *Proc. Natl. Inst. Sci. India*, 2, 49–55, 1936.
- Mallet, M., Roger, J. C., Despiiau, S., Dubovik, O., and Putaud, J. P.: Microphysical and optical properties of aerosol particles in urban zone during ESCOMPTE, *Atmos. Res.*, 69, 73–97, 2003.

- Marais, E. A., Jacob, D. J., Jimenez, J. L., Campuzano-Jost, P., Day, D. A., Hu, W., Krechmer, J., Zhu, L., Kim, P. S., Miller, C. C., Fisher, J. A., Travis, K., Yu, K., Hanisco, T. F., Wolfe, G. M., Arkinson, H. L., Pye, H. O. T., Froyd, K. D., Liao, J., and McNeill, V. F.: Aqueous-phase mechanism for secondary organic aerosol formation from isoprene: application to the southeast United States and co-benefit of SO₂ emission controls, *Atmos. Chem. Phys.*, 16, 1603–1618, <https://doi.org/10.5194/acp-16-1603-2016>, 2016.
- McNaughton, C. S., Clarke, A. D., Howell, S. G., Pinkerton, M., Anderson, B., Thornhill, L., Hudgins, C., Winstead, E., Dibb, J. E., Scheuer, E., and Maring, H.: Results from the DC-8 Inlet Characterization Experiment (DICE): Airborne versus surface sampling of mineral dust and sea salt aerosols, *Aerosol Sci. Tech.*, 41, 136–159, doi:10.1080/02786820601118406, 2007.
- Meskhidze, Nicholas, Bethany Sutherland, Xinyi Ling, Kyle Dawson, Matthew S. Johnson, Barron Henderson, Chris A. Hostetler, and Richard A. Ferrare: Improving estimates of PM_{2.5} concentration and chemical composition by application of High Spectral Resolution Lidar (HSRL) and Creating Aerosol Types from chemistry (CATCH) algorithm, *Atmos. Environ.*, 250, 118250, 2021.
- Mikoviny, T., Kaser, L., and Wisthaler, A.: Development and characterization of a High-Temperature Proton-Transfer-Reaction Mass Spectrometer (HT-PTR-MS), *Atmos. Meas. Tech.*, 3, 537–544, <https://doi.org/10.5194/amt-3-537-2010>, 2010.
- Mischenko, M., Travis, L. D., and Lacis, A. A.: Scattering, absorption, and emission of light by small particles, Cambridge University Press, Cambridge, 2002.
- Murphy, D. M., Cziczo, D. J., Froyd, K. D., Hudson, P. K., Matthew, B. M., Middlebrook, A. M., Peltier, R. E., Sullivan, A., Thomson, D. S., and Weber, R. J.: Single-particle mass spectrometry of tropospheric aerosol particles, *J. Geophys. Res.-Atmos.*, 111, D23s32, <https://doi.org/10.1029/2006jd007340>, 2006.
- Myhre, G., Samset, B. H., Schulz, M., Balkanski, Y., Bauer, S., Bernsten, T. K., Bian, H., Bellouin, N., Chin, M., Diehl, T., Easter, R. C., Feichter, J., Ghan, S. J., Hauglustaine, D., Iversen, T., Kinne, S., Kirkevåg, A., Lamarque, J.-F., Lin, G., Liu, X., Lund, M. T., Luo, G., Ma, X., van Noije, T., Penner, J. E., Rasch, P. J., Ruiz, A., Seland, Ø., Skeie, R. B., Stier, P., Takemura, T., Tsigaridis, K., Wang, P., Wang, Z., Xu, L., Yu, H., Yu, F., Yoon, J.-H., Zhang, K., Zhang, H., and Zhou, C.: Radiative forcing of the direct aerosol effect from AeroCom Phase II simulations, *Atmos. Chem. Phys.*, 13, 1853–1877, <https://doi.org/10.5194/acp-13-1853-2013>, 2013.
- Nault, B. A., Jo, D. S., McDonald, B. C., Campuzano-Jost, P., Day, D. A., Hu, W., Schroder, J. C., Allan, J., Blake, D. R., Canagaratna, M. R., Coe, H., Coggon, M. M., DeCarlo, P. F., Diskin, G. S., Dunmore, R., Flocke, F., Fried, A., Gilman, J. B., Gkatzelis, G., Hamilton, J. F., Hanisco, T. F., Hayes, P. L., Henze, D. K., Hodzic, A., Hopkins, J., Hu, M., Huey, L. G., Jobson, B. T., Kuster, W. C., Lewis, A., Li, M., Liao, J., Nawaz, M. O., Pollack, I. B., Peischl, J., Rappenglück, B., Reeves, C. E., Richter, D., Roberts, J. M., Ryerson, T. B., Shao, M., Sommers, J. M., Walega, J., Warneke, C., Weibring, P., Wolfe, G. M., Young,

- D. E., Yuan, B., Zhang, Q., de Gouw, J. A., and Jimenez, J. L.: Secondary organic aerosols from anthropogenic volatile organic compounds contribute substantially to air pollution mortality, *Atmos. Chem. Phys.*, 21, 11201–11224, <https://doi.org/10.5194/acp-21-11201-2021>, 2021
- 510 Niu, T., Gong, S. L., Zhu, G. F., Liu, H. L., Hu, X. Q., Zhou, C. H., and Wang, Y. Q.: Data assimilation of dust aerosol observations for the CUACE/dust forecasting system, *Atmos. Chem. Phys.*, 8, 3473–3482, <https://doi.org/10.5194/acp-8-3473-2008>, 2008.
- Nowottnick, E. P., Colarco, P. R., Welton, E. J., and da Silva, A.: Use of the CALIOP vertical feature mask for evaluating global aerosol models, *Atmos. Meas. Tech.*, 8, 3647–3669, <https://doi.org/10.5194/amt-8-3647-2015>, 2015.
- 515 Omar, A. H., Winker, D. M., Kittaka, C., Vaughan, M. A., Liu, Z. Y., Hu, Y. X., Treppe, C. R., Rogers, R. R., Ferrare, R. A., Lee, K. P., Kuehn, R. E., and Hostetler, C. A.: The CALIPSO Automated Aerosol Classification and Lidar Ratio Selection Algorithm, *J. Atmos. Ocean. Tech.*, 26, 1994–2014, doi:10.1175/2009jtech1231.1, 2009.
- 520 Pagowski, M., and G. A. Grell: Experiments with the assimilation of fine aerosols using an ensemble Kalman filter, *J. Geophys. Res.-Atmos.*, 117(D21), <https://doi.org/10.1029/2012JD018333>, 2012.
- 525 Peterson, D. A., Hyer, E. J., Campbell, J. R., Fromm, M. D., Hair, J. W., Butler, C. F., and Fenn, M. A.: The 2013 Rim Fire: Implications for Predicting Extreme Fire Spread, Pyroconvection, and Smoke Emissions, *B. Am. Meteorol. Soc.*, 96, 229–247, doi:10.1175/bams-d-14-00060.1, 2015.
- 530 Perring, A.E., Schwarz, J.P., Markovic, M.Z., Fahey, D.W., Jimenez, J.L., Campuzano-Jost, P., Palm, B.D., Wisthaler, A., Mikoviny, T., Diskin, G. and Sachse, G., In situ measurements of water uptake by black carbon-containing aerosol in wildfire plumes, *J. Geophys. Res.-Atmos.*, 122(2), 1086–1097, <https://doi.org/10.1002/2016JD025688>, 2017.
- 535 Petzold, A., Ogren, J. A., Fiebig, M., Laj, P., Li, S.-M., Baltensperger, U., Holzer-Popp, T., Kinne, S., Pappalardo, G., Sugimoto, N., Wehrli, C., Wiedensohler, A., and Zhang, X.-Y.: Recommendations for reporting "black carbon" measurements, *Atmos. Chem. Phys.*, 13, 8365–8379, <https://doi.org/10.5194/acp-13-8365-2013>, 2013.
- 540 Pope, C., Burnett, R., Thun, M., Calle, E., Krewski, D., Ito, K., and Thurston, G.: Lung cancer, cardiopulmonary mortality, and long-term exposure to fine particulate air pollution, *JAMA-J. Am. Med. Assoc.*, 287, 1132–1141, doi:10.1001/jama.287.9.1132, 2002.
- 545 Randles, C. A., Kinne, S., Myhre, G., Schulz, M., Stier, P., Fischer, J., Doppler, L., Highwood, E., Ryder, C., Harris, B., Huttunen, J., Ma, Y., Pinker, R. T., Mayer, B., Neubauer, D., Hittenberger, R., Oreopoulos, L., Lee, D., Pitari, G., Di Genova, G., Quaas, J., Rose, F. G., Kato, S., Rumbold, S. T., Vardavas, I., Hatzianastassiou, N., Matsoukas, C., Yu, H., Zhang, F., Zhang, H., and Lu, P.: Intercomparison of

- shortwave radiative transfer schemes in global aerosol modeling: results from the AeroCom Radiative Transfer Experiment, *Atmos. Chem. Phys.*, 13, 2347–2379, <https://doi.org/10.5194/acp-13-2347-2013>, 2013.
- Reid, J. S., Koppmann, R., Eck, T. F., and Eleuterio, D. P.: A review of biomass burning emissions part II: intensive physical properties of biomass burning particles, *Atmos. Chem. Phys.*, 5, 799–825, <https://doi.org/10.5194/acp-5-799-2005>, 2005.
- Russell P. B., M. Kacenelenbogen, J. Livingston, O. Hasekamp, S. Burton, G. Schuster, M. Johnson, K. Knobelspiesse, J. Redemann, S. Ramchandran, and B. N. Holben, A Multi-Parameter Aerosol Classification Method and its Application to Retrievals from Spaceborne Polarimetry, *J. Geophys. Res.-Atmos.*, 119(16), 9838–9863, <https://doi.org/10.1002/2013JD021411>, 2014.
- Ryerson, T. B., Camilli, R., Kessler, J. D., Kujawinski, E. B., Reddy, C. M., Valentine, D. L., Atlas, E., Blake, D. R., de Gouw, J., Meinardi, S., Parrish, D. D., Peischl, J., Seewald, J. S., and Warneke, C.: Chemical data quantify Deepwater Horizon hydrocarbon flow rate and environmental distribution, *P. Natl. Acad. Sci. USA*, 109, 20246–20253, 2012.
- Saide, P. E., Peterson, D. A., da Silva, A., Anderson, B., Ziemba, L. D., Diskin, G., Sachse, G., Hair, J., Butler, C., Fenn, M., Jimenez, J. L., Campuzano-Jost, P., Perring, A. E., Schwarz, J. P., Markovic, M. Z., Russell, P., Redemann, J., Shinozuka, Y., Streets, D. G., Yan, F., Dibb, J., Yokelson, R., Toon, O. B., Hyer, E., and Carmichael, G. R.: Revealing important nocturnal and day-to-day variations in fire smoke emissions through a multiplatform inversion, *Geophys. Res. Lett.*, 42, 2015GL063737, <https://doi.org/10.1002/2015GL063737>, 2015.
- Schutgens, N. A. J., Miyoshi, T., Takemura, T., and Nakajima, T.: Applying an ensemble Kalman filter to the assimilation of AERONET observations in a global aerosol transport model, *Atmos. Chem. Phys.*, 10, 2561–2576, <https://doi.org/10.5194/acp-10-2561-2010>, 2010.
- Selimovic, V., Yokelson, R. J., McMeeking, G. R., and Coefield, S.: In situ measurements of trace gases, PM, and aerosol optical properties during the 2017 NW US wildfire smoke event, *Atmos. Chem. Phys.*, 19, 3905–3926, <https://doi.org/10.5194/acp-19-3905-2019>, 2019.
- Selimovic, V., Yokelson, R.J., McMeeking, G.R. and Coefield, S.: Aerosol mass and optical properties, smoke influence on O₃, and high NO₃ production rates in a western US city impacted by wildfires, *J. Geophys. Res.-Atmos.*, 125(16), e2020JD032791. <https://doi.org/10.1029/2020JD032791>, 2020.
- Sessions, W. R., Reid, J. S., Benedetti, A., Colarco, P. R., da Silva, A., Lu, S., Sekiyama, T., Tanaka, T. Y., Baldasano, J. M., Basart, S., Brooks, M. E., Eck, T. F., Iredell, M., Hansen, J. A., Jorba, O. C., Juang, H.-M. H., Lynch, P., Morcrette, J.-J., Moorthi, S., Mulcahy, J., Pradhan, Y., Razinger, M., Sampson, C. B., Wang, J., and Westphal, D. L.: Development towards a global operational aerosol consensus: basic climatological characteristics of the International Cooperative for Aerosol Prediction Multi-Model

- 590 Ensemble (ICAP-MME), *Atmos. Chem. Phys.*, 15, 335–362, <https://doi.org/10.5194/acp-15-335-2015>, 2015.
- Sekiyama, T. T., Tanaka, T. Y., Shimizu, A., and Miyoshi, T.: Data assimilation of CALIPSO aerosol observations, *Atmos. Chem. Phys.*, 10, 39–49, <https://doi.org/10.5194/acp-10-39-2010>, 2010.
- 595 Shingler, T., Crosbie, E., Ortega, A., Shiraiwa, M., Zuend, A., Beyersdorf, A., Ziemba, L., Anderson, B., Thornhill, L., Perring, A.E. and Schwarz, J.P.: Airborne characterization of subsaturated aerosol hygroscopicity and dry refractive index from the surface to 6.5 km during the SEAC4RS campaign, *J. Geophys. Res.-Atmos.*, 121(8), 4188–4210, <https://doi.org/10.1002/2015JD024498>, 2016.
- 600 Stier, P., Schutgens, N. A. J., Bellouin, N., Bian, H., Boucher, O., Chin, M., Ghan, S., Huneeus, N., Kinne, S., Lin, G., Ma, X., Myhre, G., Penner, J. E., Randles, C. A., Samset, B., Schulz, M., Takemura, T., Yu, F., Yu, H., and Zhou, C.: Host model uncertainties in aerosol radiative forcing estimates: results from the AeroCom Prescribed intercomparison study, *Atmos. Chem. Phys.*, 13, 3245–3270, <https://doi.org/10.5194/acp-13-3245-2013>, 2013.
- 605 Stirnberg, R., Cermak, J., Fuchs, J. and Andersen, H.: Mapping and understanding patterns of air quality using satellite data and machine learning. *J. Geophys. Res.-Atmos.*, 125(4), e2019JD031380, <https://doi.org/10.1029/2019JD031380>, 2020.
- 610 Sorooshian, A., Hersey, S., Brechtel, F. J., Corless, A., Flagan, R. C., and Seinfeld, J. H.: Rapid, size-resolved aerosol hygroscopic growth measurements: differential aerosol sizing and hygroscopicity spectrometer probe (DASH-SP), *Aerosol Sci. Technol.*, 42, 445–464, doi:10.1080/02786820802178506, 2008.
- 615 Taylor, M., S. Kazadzis, V. Amiridis, and R. A. Kahn: Global aerosol mixtures and their multiyear and seasonal characteristics, *Atmos. Environ.*, 116, 112–129, 2015
- 620 Thorsen, Tyler J., David M. Winker, and Richard A. Ferrare: Uncertainty in observational estimates of the aerosol direct radiative effect and forcing, *J. Climate*, 34(1), 195–214, <https://doi.org/10.1175/JCLI-D-19-1009.1>, 2021.
- 625 Toon, O.B., Maring, H., Dibb, J., Ferrare, R., Jacob, D.J., Jensen, E.J., Luo, Z.J., Mace, G.G., Pan, L.L., Pfister, L. and Rosenlof, K.H.: Planning, implementation, and scientific goals of the Studies of Emissions and Atmospheric Composition, Clouds and Climate Coupling by Regional Surveys (SEAC4RS) field mission, *J. Geophys. Res.-Atmos.*, 121(9), 4967–5009, <https://doi.org/10.1002/2015JD024297>, 2016.
- 630 Tsikerdekis, A., Schutgens, N. A. J., and Hasekamp, O. P.: Assimilating aerosol optical properties related to size and absorption from POLDER/PARASOL with an ensemble data assimilation system, *Atmos. Chem. Phys.*, 21, 2637–2674, <https://doi.org/10.5194/acp-21-2637-2021>, 2021.

- Ulbrich, I. M., Canagaratna, M. R., Zhang, Q., Worsnop, D. R., and Jimenez, J. L.: Interpretation of organic components from Positive Matrix Factorization of aerosol mass spectrometric data, *Atmos. Chem. Phys.*, 9, 2891–2918, <https://doi.org/10.5194/acp-9-2891-2009>, 2009.
- 635 Uno, I., Yumimoto, K., Shimizu, A., Hara, Y., Sugimoto, N., Wang, Z., Liu, Z., and Winker, D. M.: 3-D structure of Asian dust transport revealed by CALIPSO lidar and a 4DVAR dust model, *Geophys. Res. Lett.*, 35, L06803, [doi:10.1029/2007GL032329](https://doi.org/10.1029/2007GL032329), 2008.
- 640 US EPA, The Benefits and Costs of the Clean Air Act from 1990 to 2020, Final Report – Rev. A, U.S. Environmental Protection Agency, Office of Air and Radiation, April 2011, https://www.epa.gov/sites/production/files/2015-07/documents/fullreport_rev_a.pdf, 2011.
- US EPA, Our Nation’s Air: Status and Trends Through 2015, U.S. Environmental Protection Agency,
645 <https://gispub.epa.gov/air/trendsreport/2016/>, 2016.
- Wagner, N. L., Brock, C. A., Angevine, W. M., Beyersdorf, A., Campuzano-Jost, P., Day, D., de Gouw, J. A., Diskin, G. S., Gordon, T. D., Graus, M. G., Holloway, J. S., Huey, G., Jimenez, J. L., Lack, D. A., Liao, J., Liu, X., Markovic, M. Z., Middlebrook, A. M., Mikoviny, T., Peischl, J., Perring, A. E.,
650 Richardson, M. S., Ryerson, T. B., Schwarz, J. P., Warneke, C., Welti, A., Wisthaler, A., Ziemba, L. D., and Murphy, D. M.: In situ vertical profiles of aerosol extinction, mass, and composition over the southeast United States during SENEX and SEAC⁴RS: observations of a modest aerosol enhancement aloft, *Atmos. Chem. Phys.*, 15, 7085–7102, <https://doi.org/10.5194/acp-15-7085-2015>, 2015.
- 655 Weber, R. J., Sullivan, A. P., Peltier, R. E., Russell, A., Yan, B., Zheng, M., de Gouw, J., Warneke, C., Brock, C., Holloway, J. S., Atlas, E. L., and Edgerton, E.: A study of secondary organic aerosol formation in the anthropogenic-influenced southeastern United States, *J. Geophys. Res.-Atmos.*, 112(D13), <https://doi.org/10.1029/2007JD008408>, 2007.
- 660 Werdell, P. J., Behrenfeld, M. J., Bontempi, P. S., Boss, E., Cairns, B., Davis, G. T., Franz, B. A., Gliese, U. B., Gorman, E. T., and Hasekamp, O.: The plankton, aerosol, cloud, ocean ecosystem mission: status, science, advances, *B. Am. Meteorol. Soc.*, 100, 1775–1794, 2019.
- Xu, L., Suresh, S., Guo, H., Weber, R. J., and Ng, N. L.: Aerosol characterization over the southeastern
665 United States using high-resolution aerosol mass spectrometry: spatial and seasonal variation of aerosol composition and sources with a focus on organic nitrates, *Atmos. Chem. Phys.*, 15, 7307–7336, <https://doi.org/10.5194/acp-15-7307-2015>, 2015.
- Yu, H., R. E. Dickinson, M. Chin, Y. J. Kaufman, B. N. Holben, I. V. Geogdzhayev, and M. I.
670 Mishchenko: Annual cycle of global distributions of aerosol optical depth from integration of MODIS retrievals and GOCART model simulations, *J. Geophys. Res.-Atmos.*, 108(D3), <https://doi.org/10.1029/2002JD002717>, 2003.

- 675 Yumimoto, K., Uno, I., Sugimoto, N., Shimizu, A., Liu, Z., and Winker, D. M.: Adjoint inversion
modeling of Asian dust emission using lidar observations, *Atmos. Chem. Phys.*, 8, 2869–2884,
<https://doi.org/10.5194/acp-8-2869-2008>, 2008.
- 680 Wichmann, H. E., Spix, C., Tuch, T., Wölke, G., Peters, A., and Heinrich, J.: Daily mortality and fine and
ultrafine particles in Erfurt, Germany, part I: role of particle number and particle mass, *Res. Rep. Health
Eff. Inst.*, 98, 5–94, 2000.
- Wu, X., Braun, D., Schwartz, J., Kioumourtzoglou, M. A., and Dominici, F.: Evaluating the impact of
long-term exposure to fine particulate matter on mortality among the elderly, *Sci. Adv.*, 6(29), eaba5692,
doi: 10.1126/sciadv.aba5692, 2020.
- 685 Zhang, J., J. S. Reid, D. L. Westphal, N. L. Baker, and E. J. Hyer: A system for operational aerosol optical
depth data assimilation over global oceans, *J. Geophys. Res.-Atmos.*, 113(D10),
<https://doi.org/10.1029/2007JD009065>, 2008.
- 690 Zhang, J., Campbell, J. R., Reid, J. S., Westphal, D. L., Baker, N. L., Campbell, W. F., and Hyer, E. J.:
Evaluating the impact of assimilating CALIOP-derived aerosol extinction profiles on a global mass
transport model, *Geophys. Res. Lett.*, 38, L14801, doi:10.1029/2011GL047737, 2011.
- 695 Zhang, H., Yee, L. D., Lee, B. H., Curtis, M. P., Worton, D. R., Isaacman-VanWertz, G., Offenberg, J.
H., Lewandowski, M., Kleindienst, T. E., Beaver, M. R., Holder, A. L., Lonneman, W. A., Docherty, K.
S., Jaoui, M., Pye, H. O. T., Hu, W., Day, D. A., Campuzano-Jost, P., Jimenez, J. L., Guo, H., Weber, R.
J., Gouw, J. de, Koss, A. R., Edgerton, E. S., Brune, W., Mohr, C., Lopez-Hilfiker, F. D., Lutz, A.,
Kreisberg, N. M., Spielman, S. R., Hering, S. V., Wilson, K. R., Thornton, J. A., and Goldstein, A. H.:
Monoterpenes are the largest source of summertime organic aerosol in the southeastern United States, *P.
700 Natl. Acad. Sci. USA*, 115, 2038–2043, <https://doi.org/10.1073/pnas.1717513115>, 2018.
- Ziemba, L. D., Hudgins, C. H., Obland, M. D., Rogers, R. R., Scarino, A. J., Winstead, E. L., Anderson,
B. E., Thornhill, K. L., Ferrare, R., Barrick, J., Beyersdorf, A. J., Chen, G., Crumeyrolle, S., Hair, J., and
Hostetler, C. A.: Airborne observations of aerosol extinction by in situ and remote-sensing techniques:
705 Evaluation of particle hygroscopicity, *Geophys. Res. Lett.*, 40, 417–422, doi:10.1029/2012GL054428,
2013